Supplementary Information for

Continuous photo-oxidation of methane to methanol at an atomically tailored reticular gas-solid interface

Yuchen Hao[1]†*, Liwei Chen[2,3]†, Haodong Liu[1], Wenfeng Nie[1], Xiangjie Ge[1], Jiani Li[2], Hui-Zi Huang[2], Chao Sun[2], Cuncai Lv[1], Shangbo Ning[1], Linjie Gao[1], Yaguang Li[1], Shufang Wang[1], An-Xiang Yin[2], Bo Wang[2]* and Jinhua Ye[1]*

Corresponding author: haoyc@hbu.edu.cn (Y.C.H.); bowang@bit.edu.cn (B.W.); jinhua.YE@nims.go.jp (J.H.Y.)

The PDF file includes:

Supplementary Figs. 1 to 60
Supplementary Tables 1 to 5
References

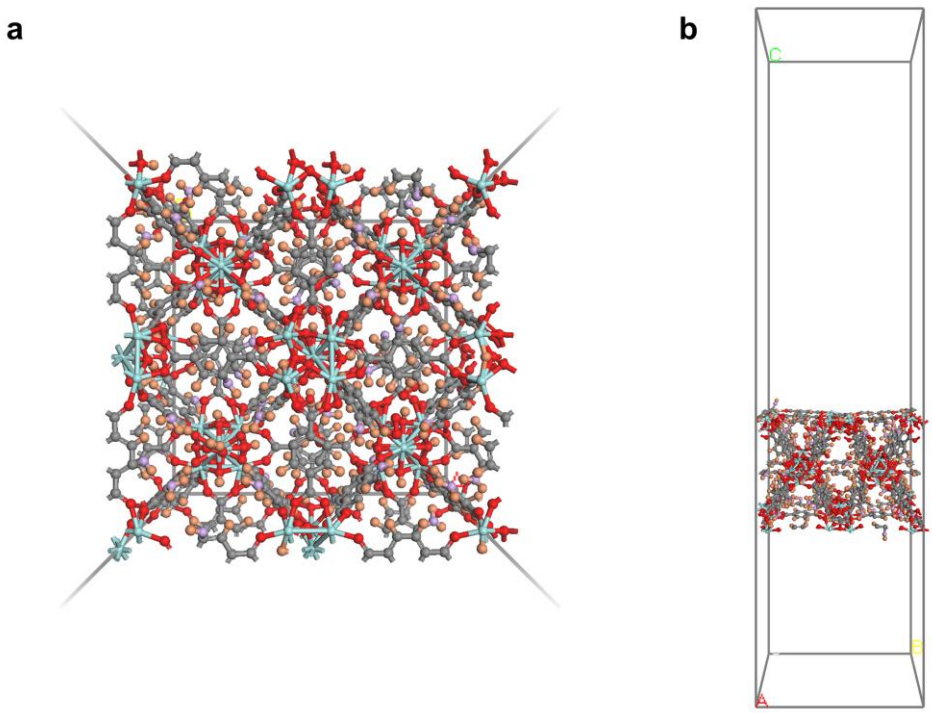

Supplementary Fig. 1: Structural illustrations of the NH_2-UiO-66 (aUiO) membrane considered in this work. NH_2-UiO-66 structures are represented as sticks with color codes of carbon: grey, oxygen: red, hydrogen: orange, zirconium: cyan, and nitrogen: violet.

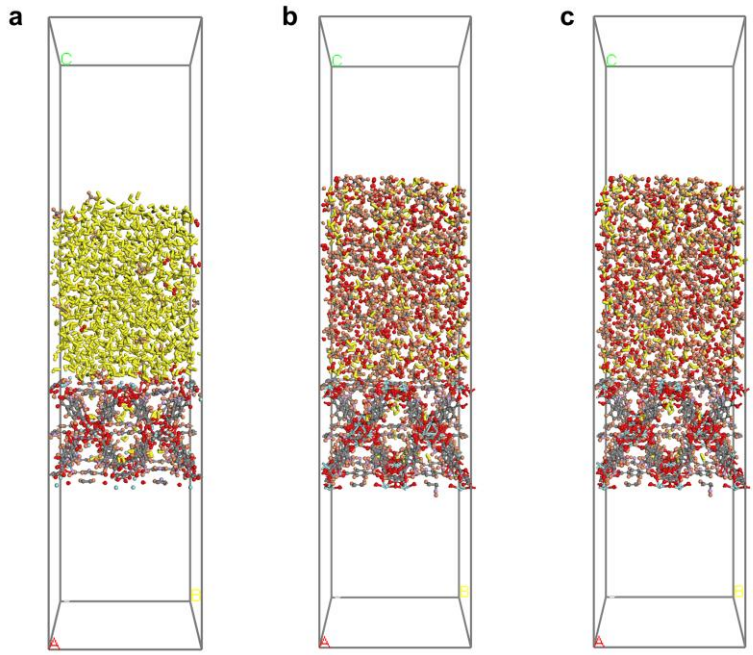

Supplementary Fig. 2: Schematic illustration of the MD simulation system. (**a**) Liquid-solid system (298 K). (**b**) Gas-solid system (298 K). (**c**) Gas-solid system (348 K).

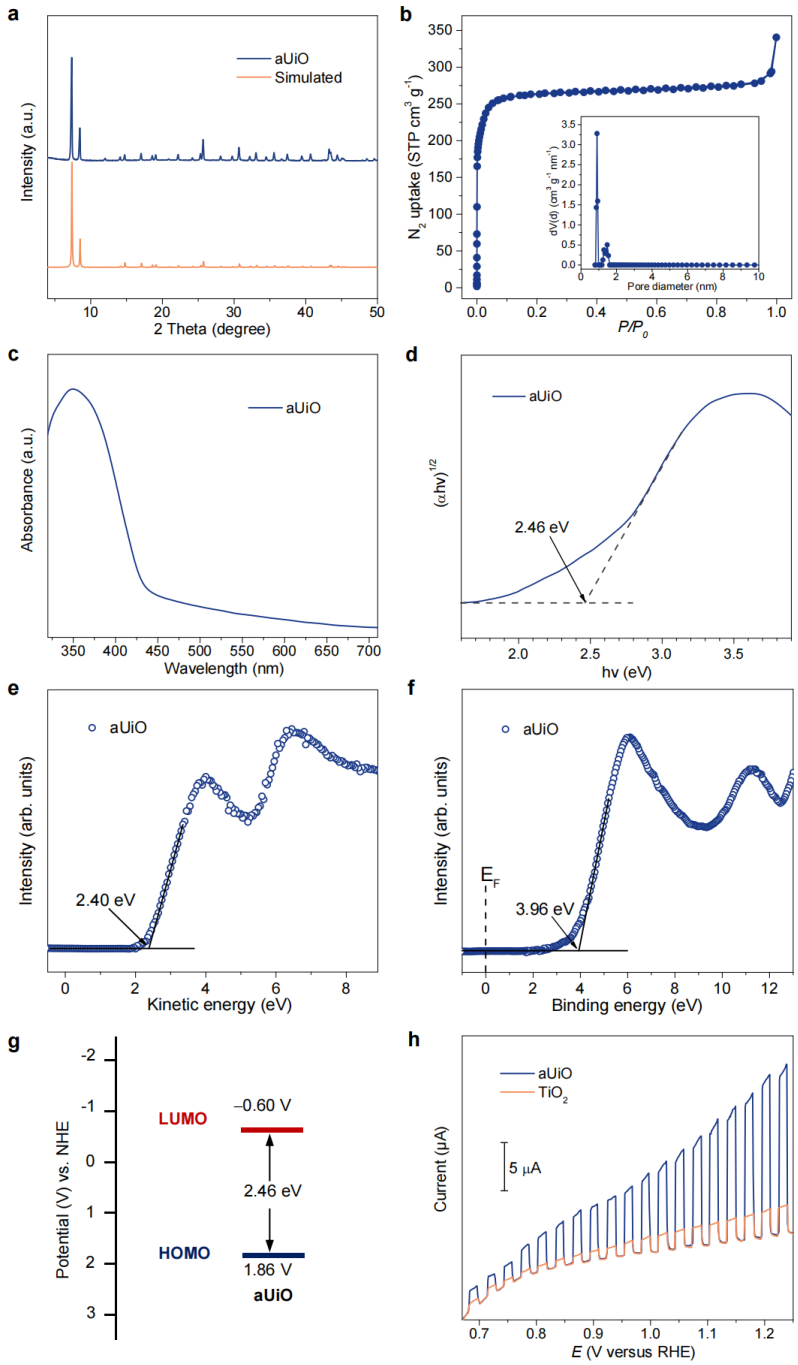

Supplementary Fig. 3: Characterization of NH_2-UiO-66 (aUiO) particles. (**a**) XRD pattern, (**b**) N_2 adsorption-desorption isotherms (at 77 K) and pore size distribution (inset), (**c**) UV-vis diffuse reflectance spectra of aUiO. (**d**) Optical band gap determined by UV-vis diffuse reflectance, where α and ν represent the absorbance and wavenumber, respectively. (**e**) Valence-band spectra for aUiO measured by ultraviolet photoelectron spectroscopy (UPS). Au serves as a reference for EF set to 0 eV. (**f**) Secondary electron cutoff (E_{cutoff}) in the UPS spectra, from which the work function (Φ) can be calculated. (**g**) Schematic diagrams for conduction band gap of the aUiO. (**h**) Photocurrent-potential curve for aUiO and commercial TiO_2. The TiO_2 powders were purchased from Energy Chemical (China).

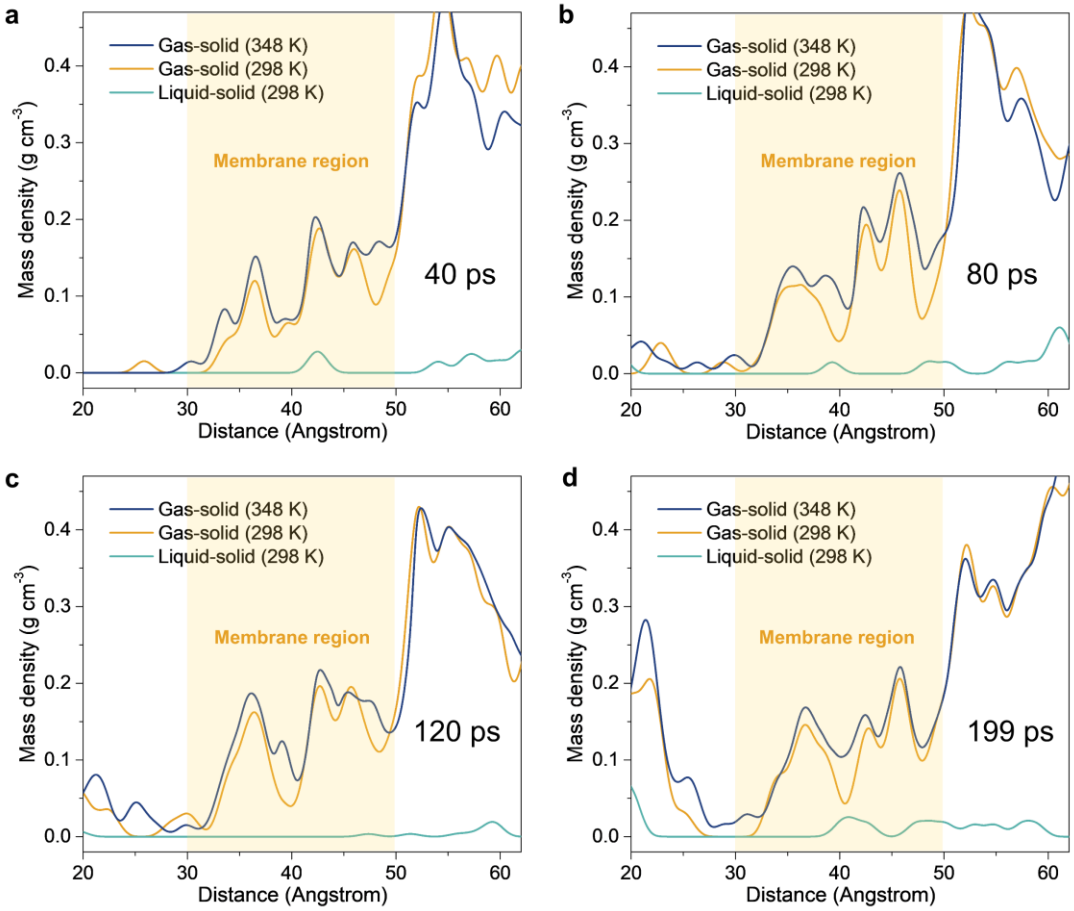

Supplementary Fig. 4: Mass density profiles of CH_4 in the gas-solid (298K and 348K) and liquid-solid (298 K) systems along the gas diffusion (gas-solid system) or water flow (liquid-solid system) direction under different simulation times. (**a**) 40 ps. (**b**) 80 ps. (**c**) 120 ps. (**d**) 199 ps.

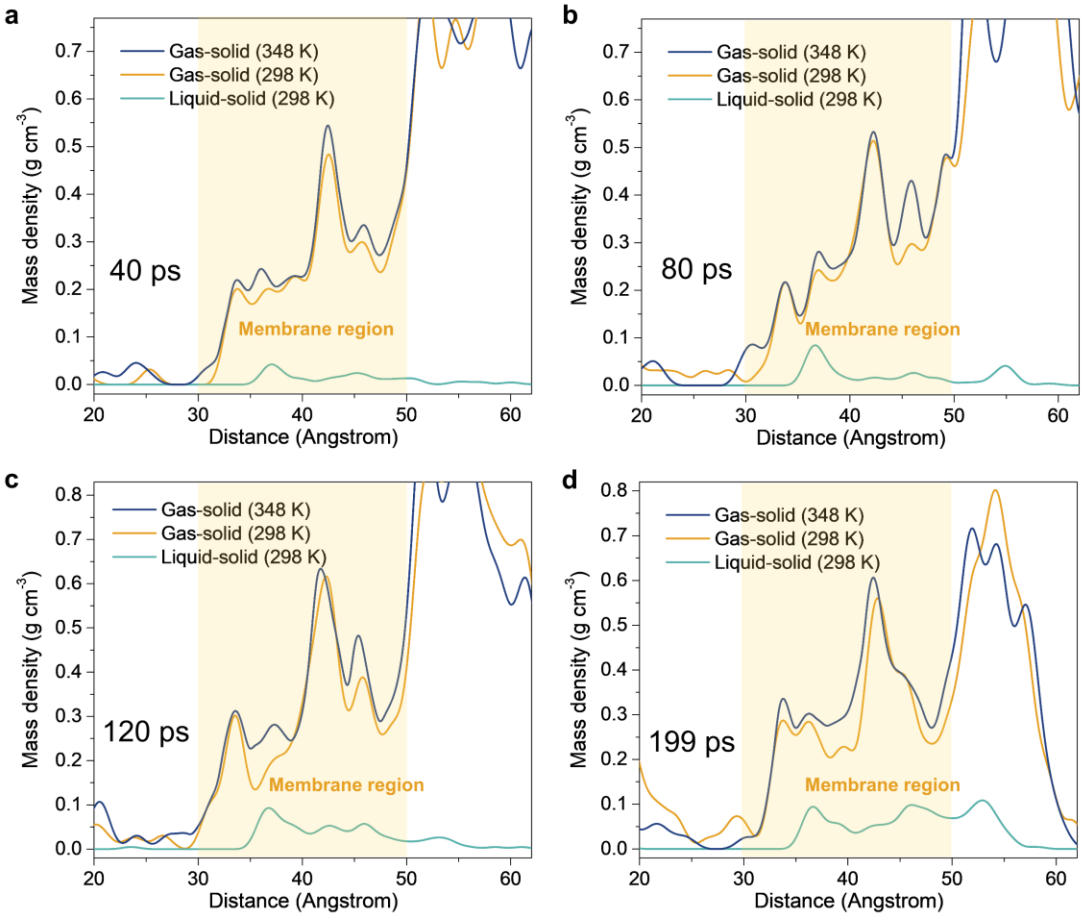

Supplementary Fig. 5: Mass density profiles of O_2 in the gas-solid (298K and 348K) and liquid-solid (298 K) systems along the gas diffusion (gas-solid system) or water flow (liquid-solid system) direction under different simulation times. (**a**) 40 ps. (**b**) 80 ps. (**c**) 120 ps. (**d**) 199 ps.

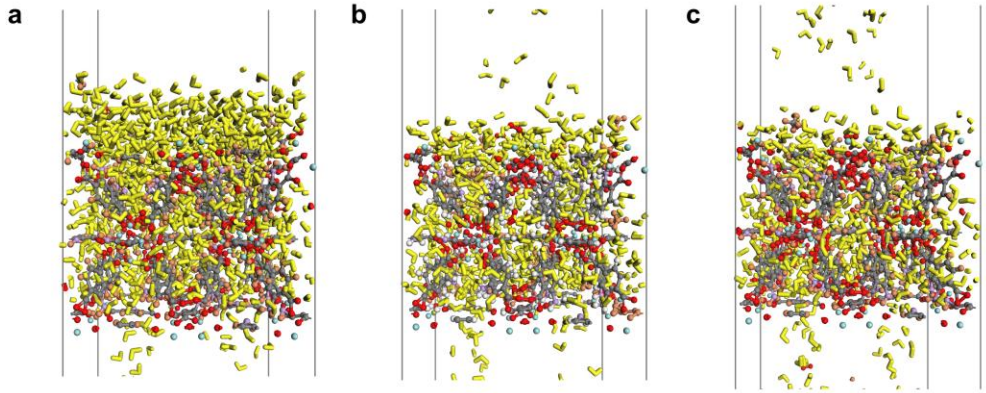

Supplementary Fig. 6: Snapshots of the water molecule distribution in the liquid-solid system (298 K, water molecules are highlighted as the yellow sticks). In the PTMO process, water would flood the pores of the MOF membrane, rapidly diluting the in situ generated H_2O_2.

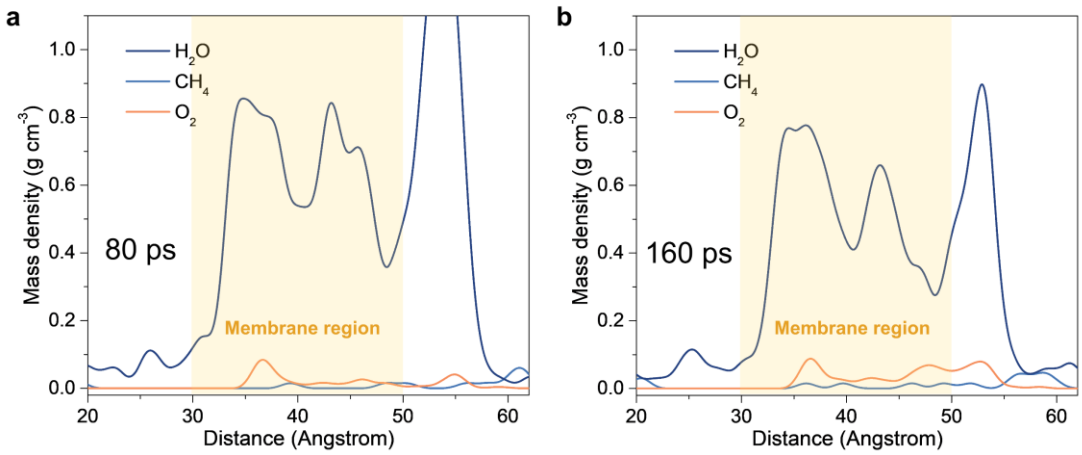

Supplementary Fig. 7: Mass density profiles of H_2O, CH_4, and O_2 in the liquid-solid system along the water flow direction. (**a**) Under 80 ps simulation. (**b**) Under 160 ps simulation.

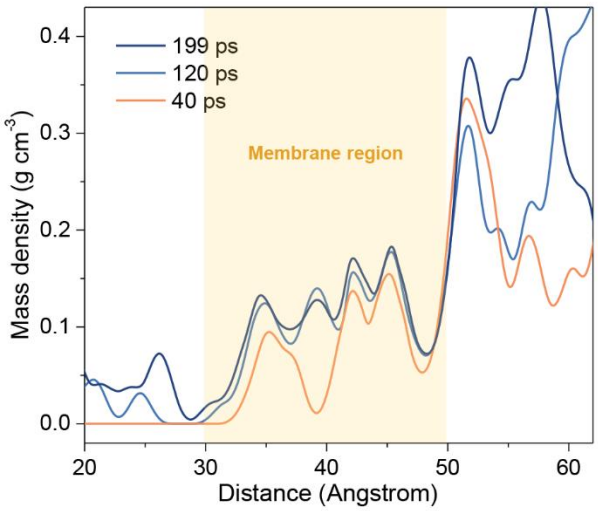

Supplementary Fig. 8: Mass density profiles of water molecules in the gas-solid system (at 298 K) along the gas diffusion direction under different simulation times. With the prolonged operation of the gas-solid PTMO system under ambient temperature (25 ^{o}C), water molecules accumulate increasingly within the pores of the aUiO membrane.

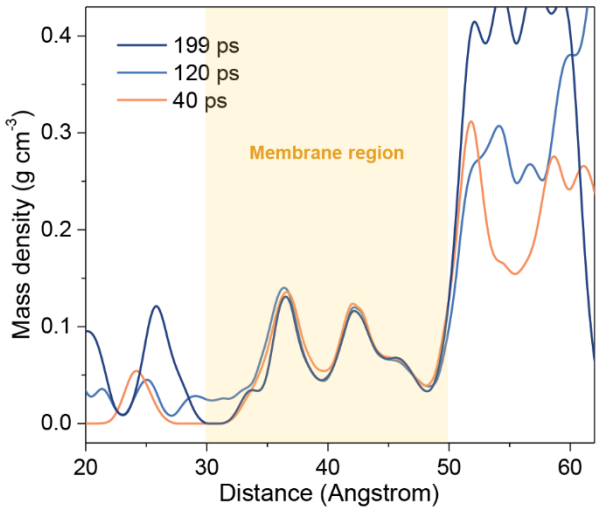

Supplementary Fig. 9: Mass density profiles of water molecules in the gas-solid system (at 348 K) along the gas diffusion direction under different simulation times. Elevating the system temperature can effectively remove stagnant water from the MOF pores, ensuring a clear gas-solid interface without vapor retention and/or condensation during the simulation.

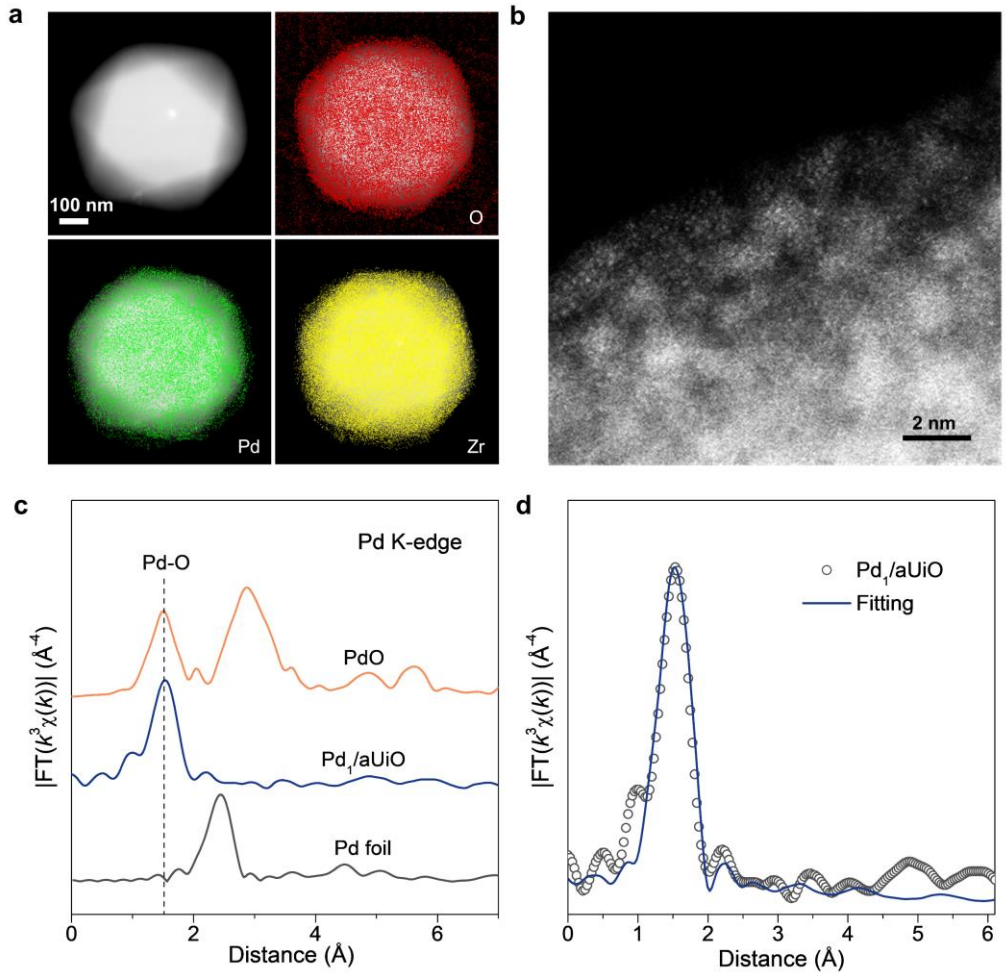

Supplementary Fig. 10: Structural characterization of the as-prepared Pd_1/aUiO particles. (**a**) STEM image and corresponding EDS maps for Pd_1/aUiO particles. (**b**) AC-HAADF-STEM image for Pd_1/aUiO particles. (**c**) Pd K-edge EXAFS spectra of Pd_1/aUiO, PdO, and Pd foil. (**d**) Pd K-edge EXAFS fitting results for Pd_1/ aUiO. The presence of Pd–O coordination but no Pd–Pd signals confirmed the atomic dispersion of Pd species in the 0.78 wt.% Pd_1/aUiO samples.

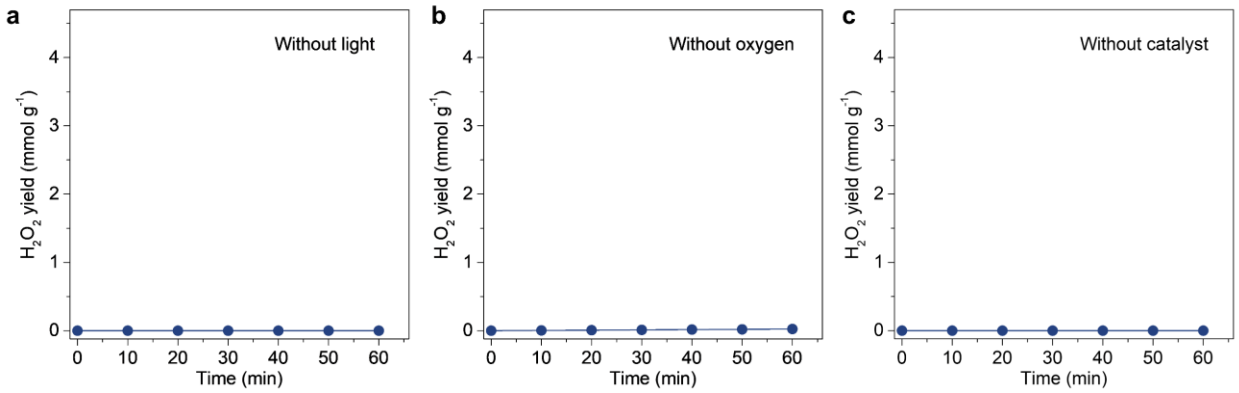

Supplementary Fig. 11: Blank experiments for POR on Pd_1/aUiO powders. No H_2O_2 evolution could be detected in POR experiments without (**a**) light irradiation, (**b**) O_2 feed, or (**c**) photocatalysts.

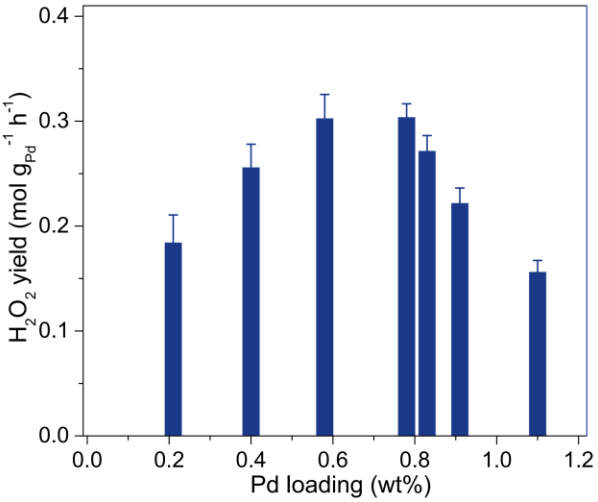

Supplementary Fig. 12: H_2O_2 yield as a function of Pd loadings in Pd/aUiO catalysts (reaction condition: 80 mL min^{-1} O_2, 25 °C, triethanolamine was used as a scavenger for the photogenerated hole). The error bars correspond to the standard deviation of three independent measurements.

Note: When the Pd loading was below 0.78 wt.%, the photocatalytic activity for H_2O_2 generation increased with higher Pd loading, attributed to the growing number of Pd_1 active sites. However, at higher loading contents of Pd (e.g., 0.83 wt.% or above), Pd atoms aggregated, forming metallic Pd species. These metallic species exhibited significantly reduced intrinsic activity for O_2 reduction to H_2O_2, resulting in a marked decline in H_2O_2 yield.

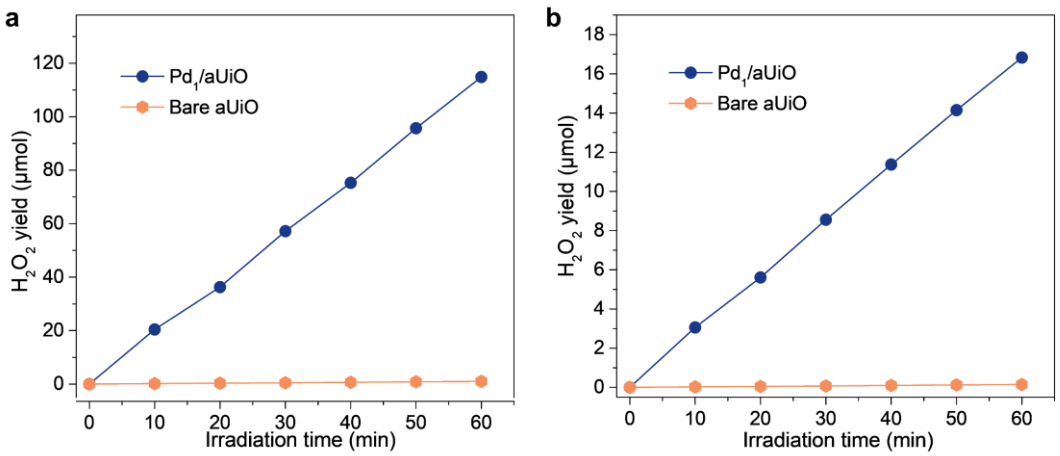

Supplementary Fig. 13: Time course of H_2O_2 evolution on Pd_1/aUiO and bare aUiO catalysts under simulated sunlight irradiation (AM 1.5G) with (**a**) and without (**b**) triethanolamine (TEA) as the sacrificial agent.

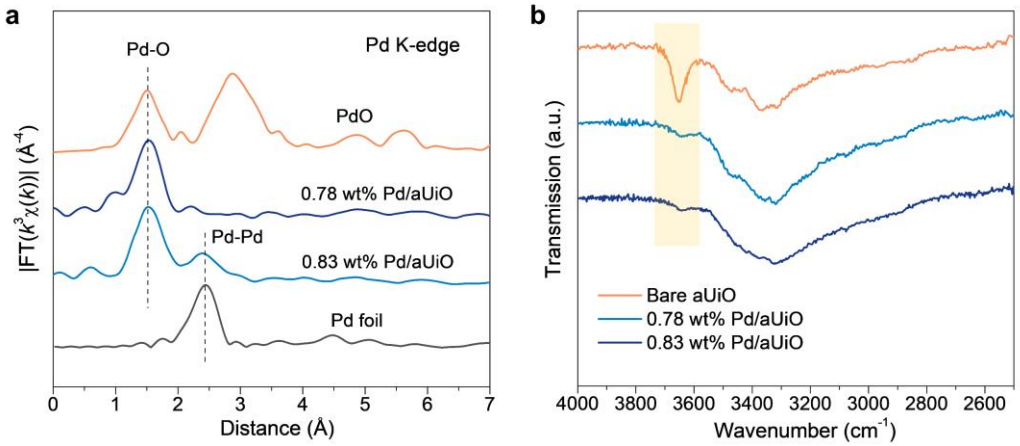

Supplementary Fig. 14: (**a**) Pd K-edge EXAFS spectra of 0.78 wt.% Pd_1/aUiO, 0.83 wt.% Pd/aUiO, PdO, and bulk Pd foil. (**b**) DRIFTS spectra of bare aUiO, 0.78 wt.% Pd_1/aUiO and 0.83 wt.% Pd/aUiO catalysts. The presence of $-O/OH_x$ vibration in the post-activation aUiO samples suggests the effective removal of coordinated acetates from the Zr–O nodes through a high dynamical vacuum activation process, resulting in aUiO particles with missing linkers and Zr–O nodes with abundant defects terminated by $-O/-OH_x$ groups. The significant decrease in peak intensity of $-O/OH_x$ groups in DRIFTS spectra following Pd incorporation suggests these Pd species were confined on the defect sites of Zr–O nodes.

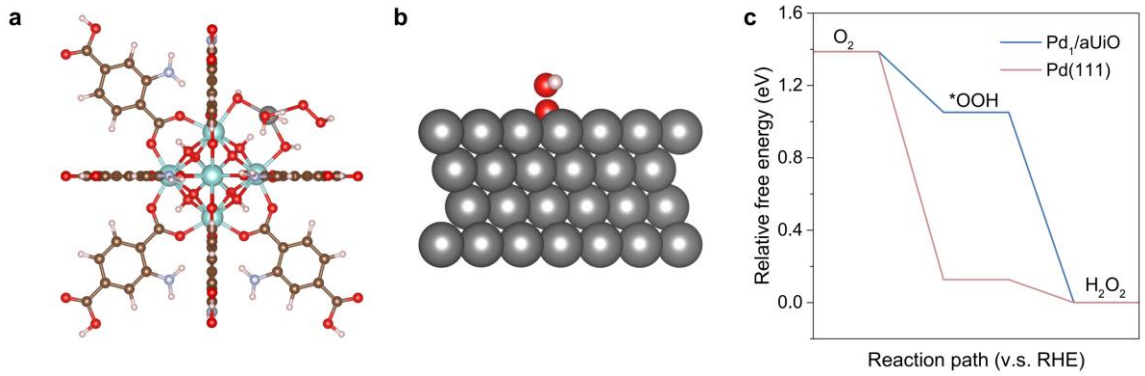

Supplementary Fig. 15: (**a**, **b**) Side views of the slab models for Pd_1/aUiO and Pd (111) facets, respectively. (**c**) Calculated potential energy diagrams for hydrogenation of O_2 to H_2O_2 on Pd_1 sites and Pd (111) surfaces.

Note: To further elucidate why single-atom Pd (Pd_1) was chosen over conventional Pd nanoparticle as H_2O_2 generation active center, we have performed first-principles calculations to investigate the formation of H_2O_2 over Pd single atom and nanoparticle. The Pd_1/aUiO(H) model is based on the palladium-oxygen coordination number fitted by EXAFS (Supplementary Fig. 15a), and the Pd nanoparticle is extracted from the bulk phase of Pd (111) (Supplementary Fig. 15b). As shown in Supplementary Fig. 15c, the rate-determining step (RDS) for O_2 reduction to generate H_2O_2 on Pd_1 sites of Pd_1/aUiO(H) is the formation of *OOH from adsorbed O_2, with a step free energy drop of 0.336 eV. In contrast, on the surface of Pd nanoparticles, the RDS is the hydrogenation of *OOH, which exhibits a smaller step free energy drop of 0.127 eV. Compared to Pd nanoparticles, Pd_1 sites effectively regulate the free energy differences at each reaction step by weakening the adsorption strength of *OOH, thereby facilitating the reaction. Overall, these calculated results suggest that Pd_1 sites are significantly more favorable than conventional Pd nanoparticles for H_2O_2 generation.

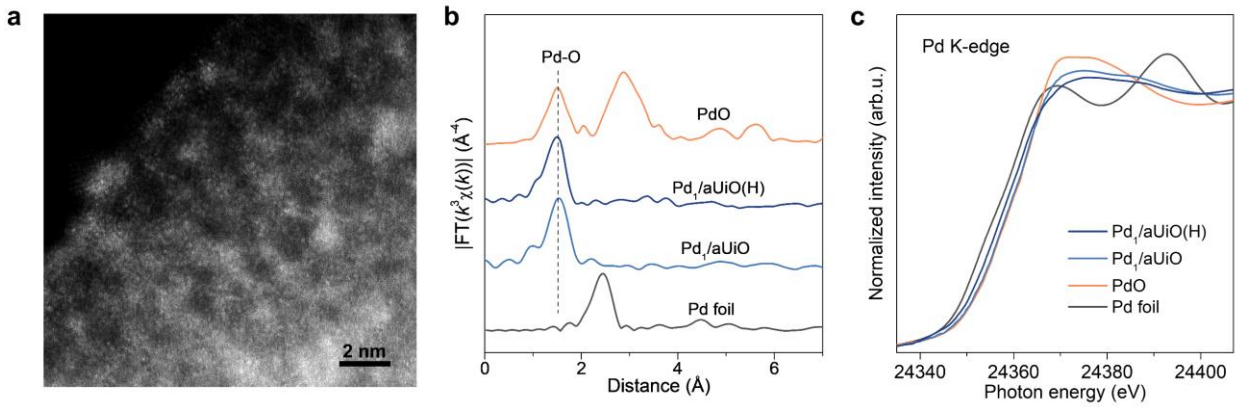

Supplementary Fig. 16: Structural characterization of the as-prepared Pd_1/aUiO(H) particles. (**a**) AC-HAADF-STEM image for Pd_1/aUiO(H) particles. (**b**) Pd K-edge EXAFS spectra of Pd_1/aUiO(H), Pd_1/aUiO, PdO, and bulk Pd foil. (**c**) Pd K-edge XANES spectra of Pd_1/aUiO(H) and Pd_1/aUiO. PdO and Pd foils were used as standard.

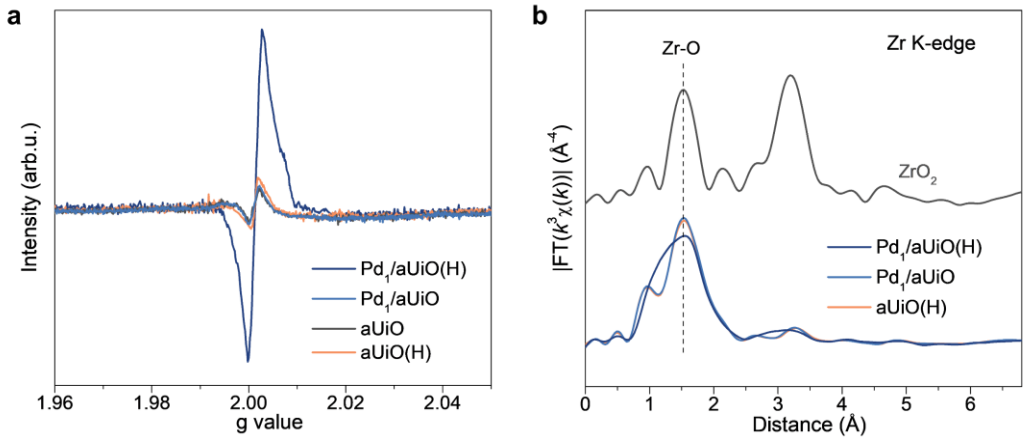

Supplementary Fig. 17: Characterization of the oxygen defects on Zr–O nodes created by Pd_1-catalyzed hydrogenation. (**a**) Electron spin resonance (ESR) profiles of Pd_1/aUiO(H), Pd_1/aUiO, aUiO(H) and aUiO under Ar atmosphere. A much stronger ESR signal was observed on the Pd_1/aUiO(H) samples, revealing a substantial increase in the density of oxygen defect sites on the Zr–O nodes of the Pd_1/aUiO(H) catalyst. The aUiO(H) catalyst was prepared by treating the as-prepared aUiO powders in H_2 (150 mL min^{-1}) gas flow at 80 °C for 10 min. (**b**) Zr K-edge FT-EXAFS spectra of Pd_1/aUiO(H), Pd_1/aUiO, aUiO(H), and aUiO, with ZrO_2 as reference. The FT-EXAFS spectrum of the Pd_1/aUiO(H) sample was measured under *Operando* hydrogenation conditions (150 mL min^{-1} H_2, 80 °C) to avoid the impact from adsorption water and/or oxygen. The structural changes in Pd_1/aUiO(H), notably the overall shrinking of the Zr–O path, suggested a diminished Zr coordination number post H_2 treatment owing to the formation of oxygen defects.

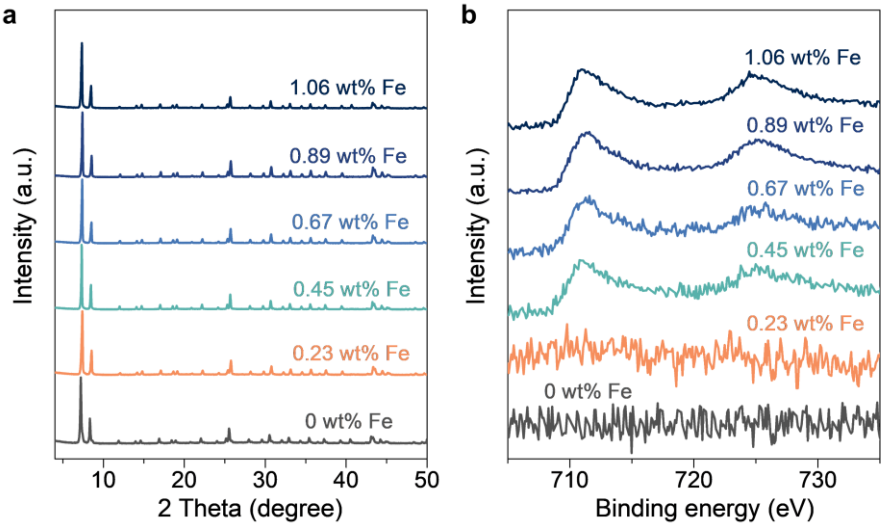

Supplementary Fig. 18: Characterization of Fe species incorporated Pd_1/aUiO(H) catalysts. (**a**) XRD patterns and (**b**) Fe 4*f* core level XPS spectra for Pd_1FeO_x/aUiO(H) catalysts with different Fe loading contents.

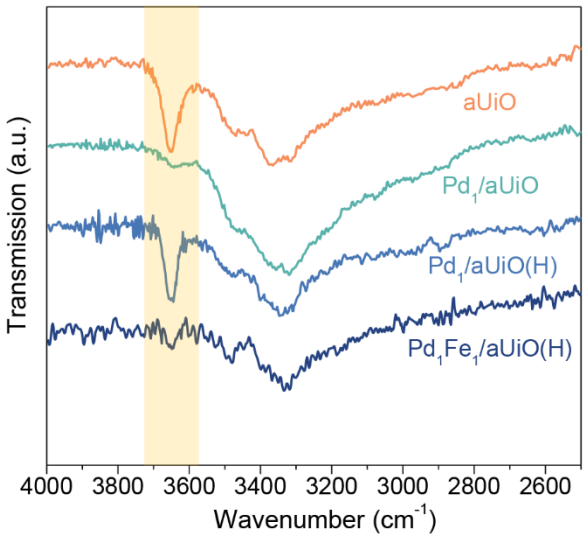

Supplementary Fig. 19: DRIFTS spectra of Pd_1Fe_1/aUiO(H), Pd_1/aUiO(H), Pd_1/aUiO, and aUiO samples. The significant decrease in the peak intensity of $-O/OH_x$ groups in DRIFTS spectra following Fe_1 species incorporation suggests that these Fe_1 were confined on the defect sites of Zr–O nodes created by Pd_1-catalyzed hydrogenation and close to Pd_1.

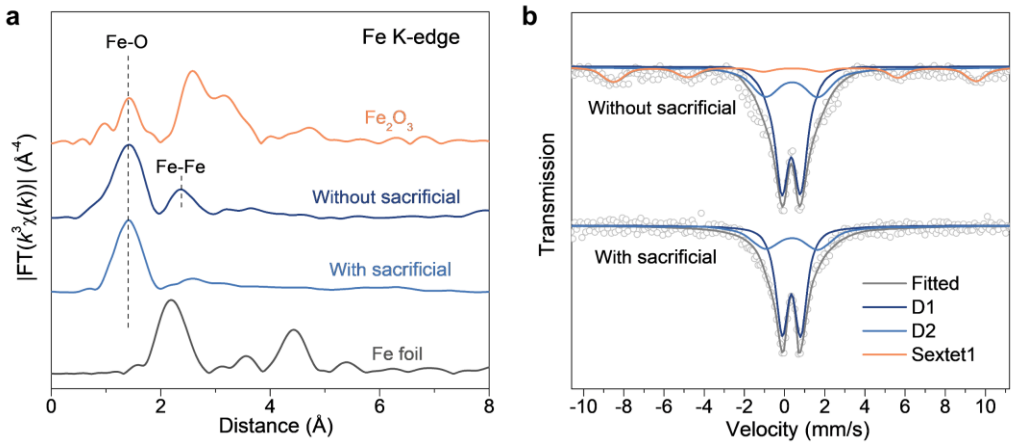

Supplementary Fig. 20: Structural characterization of the Fe species modified Pd_1/aUiO(H) catalysts synthesized with and without adding triethanolamine (TEA) as hole sacrificial. (**a**) Fe K-edge EXAFS spectra. (**b**) ^{57}Fe Mössbauer spectra. During the photo-deposition process, when triethanolamine (TEA) was used as a hole scavenger, it led to the integration of only atomically dispersed Fe species into aUiO(H), and iron oxide clusters were conspicuously absent in the resultant sample. This suggests that the iron oxide clusters within the Pd_1FeO_x/aUiO catalyst were formed by the photocatalytic oxidation of iron ions.

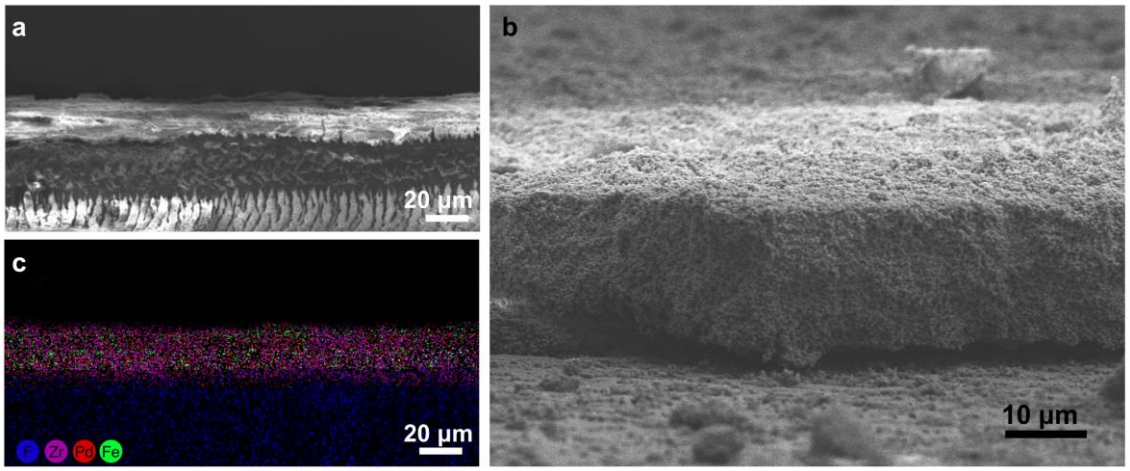

Supplementary Fig. 21: Structural characterization of the Pd_1FeO_x/aUiO(H) membranes. (**a, b**) Cross-sectional SEM images of the as-prepared Pd_1FeO_x/aUiO/PTFE membrane. (**c**) Cross-sectional EDS mapping image of the Pd_1FeO_x/aUiO/PTFE membrane corresponding to (**a**).

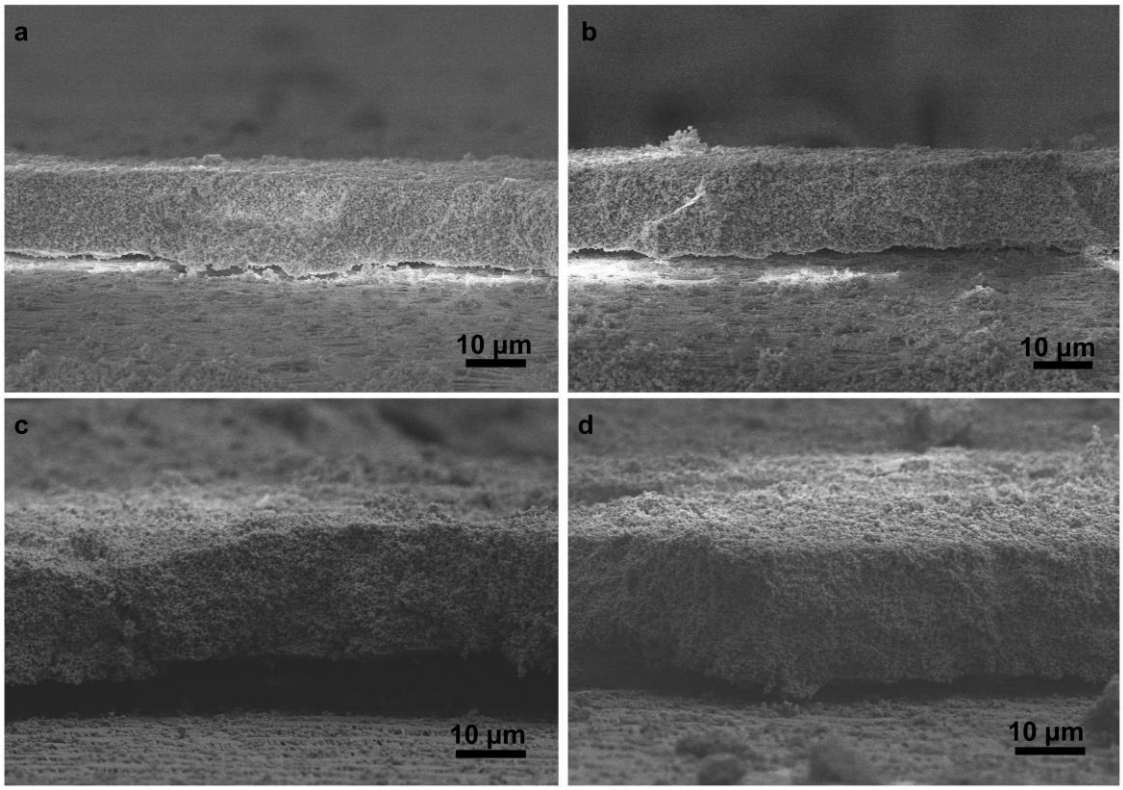

Supplementary Fig. 22: Cross-sectional SEM images of the as-prepared Pd_1FeO_x/aUiO membranes with different Fe loading contents. (**a**) 0.23 wt.%, (**b**) 0.45 wt.%, (**c**) 0.67 wt.% and (**d**) 0.89 wt.%.

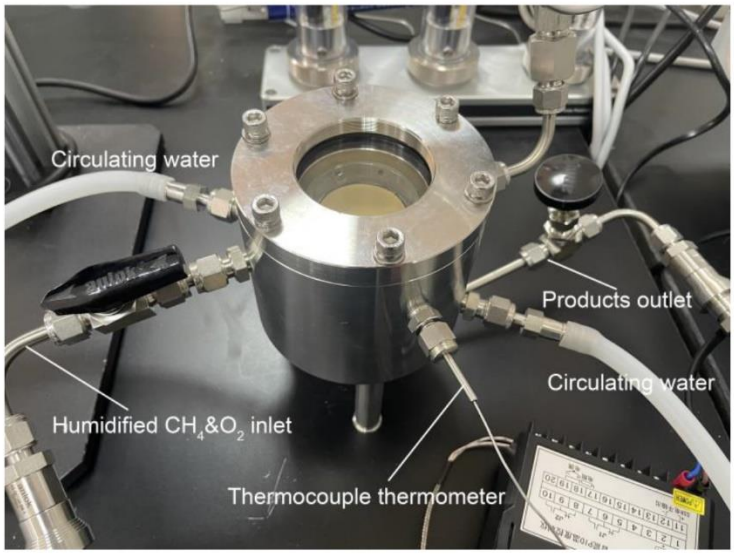

Supplementary Fig. 23: Digital photographs of the gas-flow cell used in the gas-phase PTMO experiments.

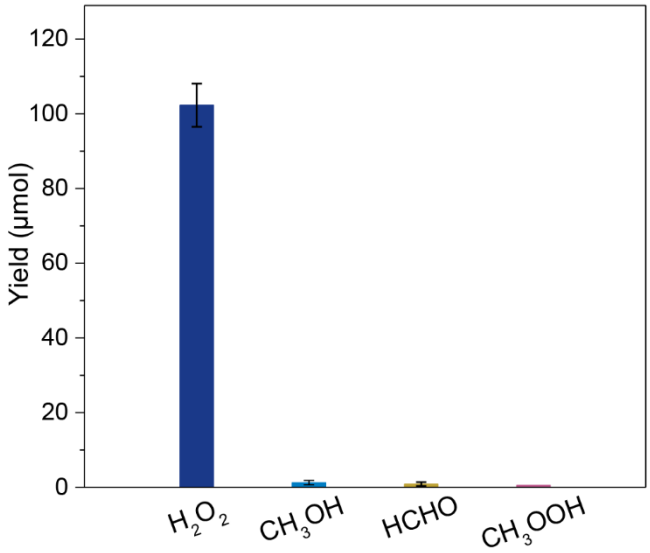

Supplementary Fig. 24: PTMO yields for different products on Pd_1/aUiO(H) membrane (reaction condition: 150 mL min^{-1} humidified CH_4/O_2 mixture gas, 25 °C, 1 hour). The error bars correspond to the standard deviation of three independent measurements.

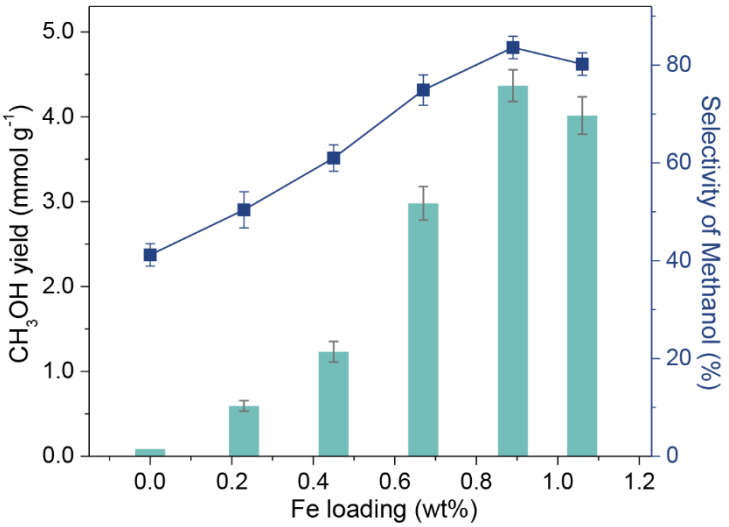

Supplementary Fig. 25: Comparison of the catalytic activity (left axis) and selectivity (right axis) for PTMO to CH_3OH on Fe species decorated Pd_1/aUiO(H) catalysts with different Fe loadings (reaction condition: 150 mL min^{-1} humidified CH_4/O_2 mixture gas, 25 °C, 1 hour). The error bars correspond to the standard deviation of three independent measurements.

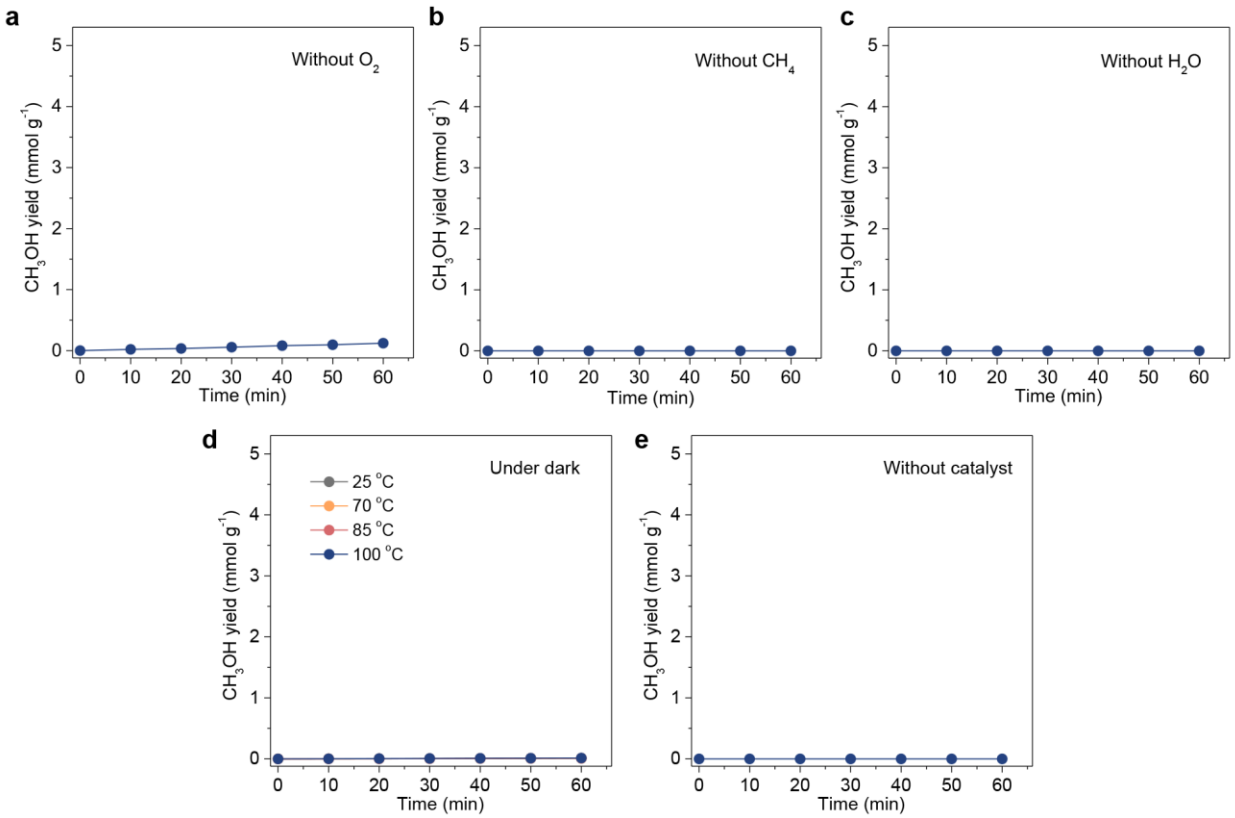

Supplementary Fig. 26: Blank experiments for PTMO on Pd_1FeO_x/aUiO membrane. No obvious CH_3OH evolution could be detected in experiments without (**a**) O_2 feed, (**b**) CH_4 feed, (**c**) water vapour, (**d**) light irradiation, or (**e**) catalysts. It is noteworthy that PTMO cannot be triggered under dark even at an elevated temperature of 100 ^oC, illustrating the light-driven rather than thermal-driven nature of PTMO.

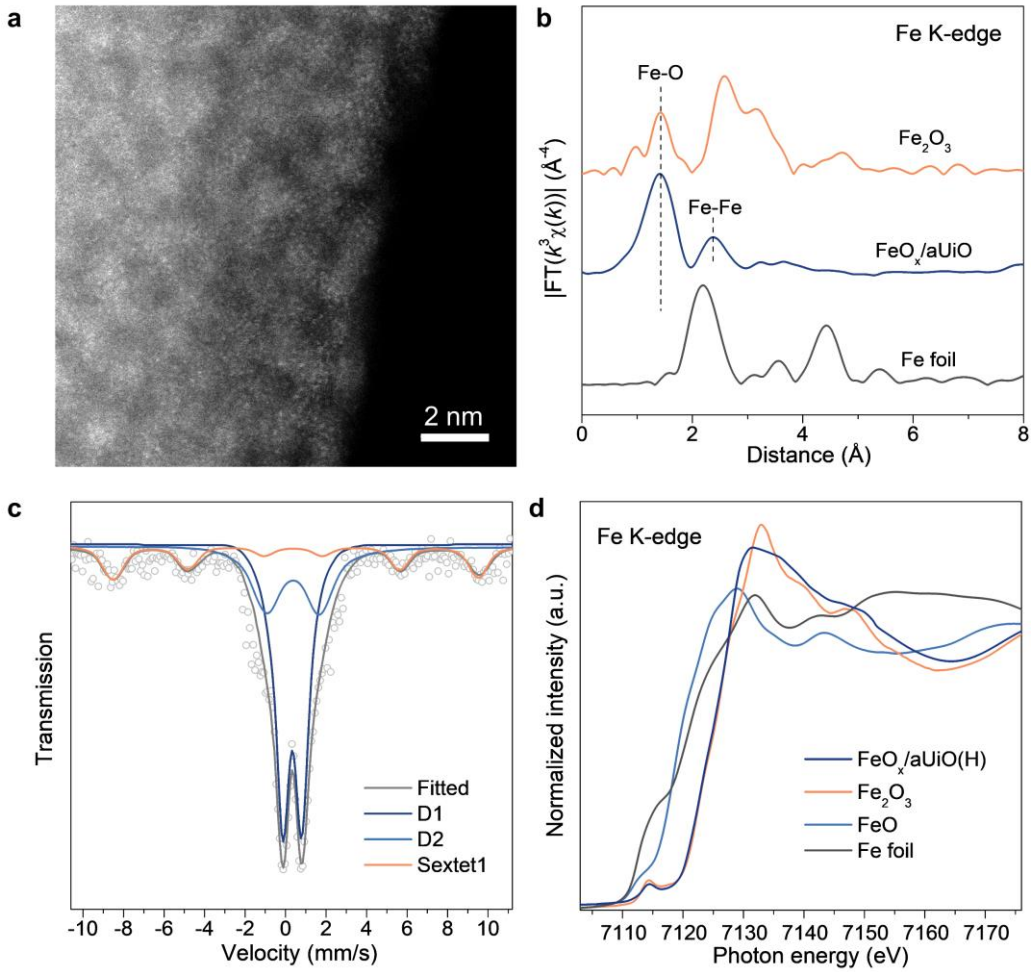

Supplementary Fig. 27: Structural characterization of the as-prepared FeO_x/aUiO(H) particles. (**a**) AC-HAADF-STEM image for FeO_x/aUiO(H) particles. (**b**) Fe K-edge EXAFS spectra of FeO_x/aUiO(H), Fe_2O_3, and Fe foil. (**c**) ^{57}Fe Mössbauer spectra of FeO_x/aUiO(H). (**d**) Fe K-edge XANES spectra of FeO_x/aUiO(H) catalyst, with Fe_2O_3, FeO, and Fe foil as references.

Note: the FeO_x/aUiO designation refers to the aUiO substrate modified with both single-atom Fe (Fe_1) and FeO_x clusters. This structure is comparable to the Pd_1FeO_x/aUiO catalyst, derived from Pd_1/UiO(H), but without the modification of Pd_1 active sites.

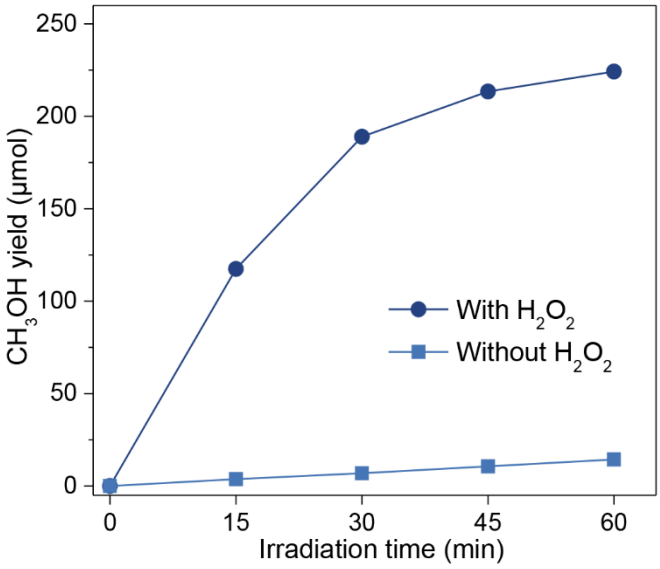

Supplementary Fig. 28: Methanol yield in the FeO_x/aUiO(H) membrane with and without adding H_2O_2 as an initiator.

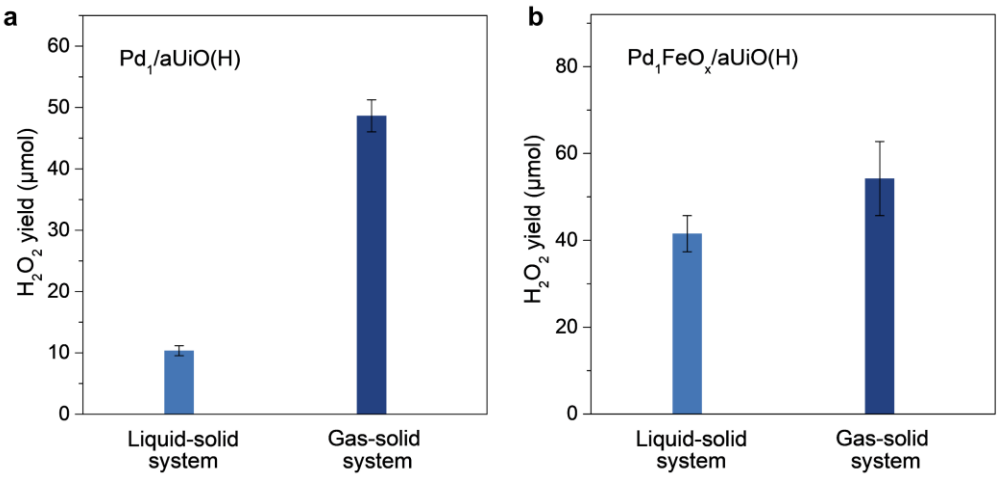

Supplementary Fig. 29: Comparison of the H_2O_2 yield in the liquid-solid and gas-solid systems (reaction condition: 150 mL min^{-1} O_2, 25 °C, 0.5 hour). (**a**) Using Pd_1/aUiO(H) as the catalyst. (**b**) Using Pd_1FeO_x/aUiO(H) as the catalyst. The error bars correspond to the standard deviation of three independent measurements.

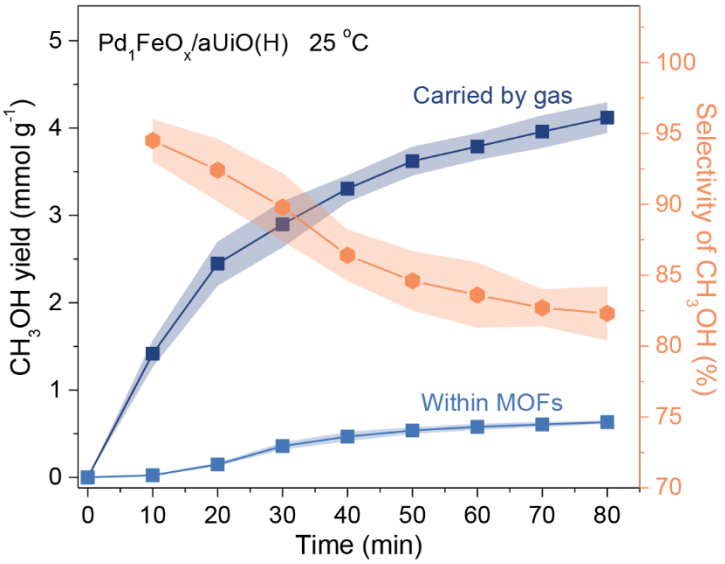

Supplementary Fig. 30: Time-on-line CH_3OH yield (left axis) and selectivity (right axis) on the Pd_1FeO_x/aUiO(H) membrane (reaction condition: 150 mL min^{-1} humidified CH_4/O_2 mixture gas, 25 °C). The error bands correspond to the standard deviation of three independent measurements.

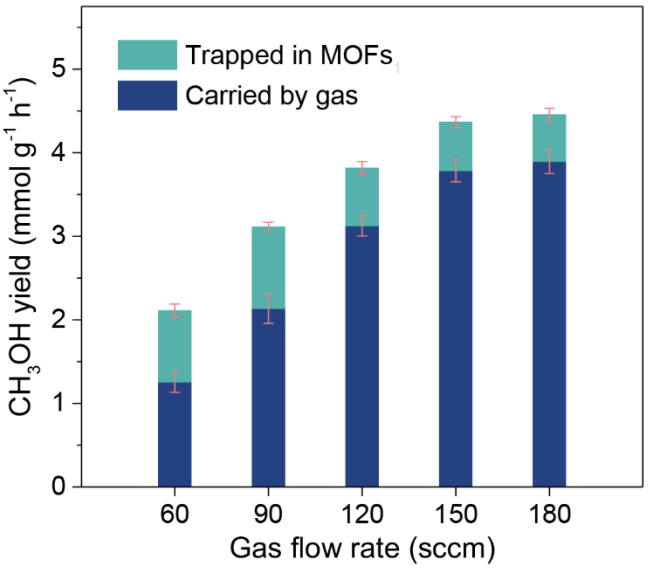

Supplementary Fig. 31: Comparison of the CH_3OH contents within (remained in MOF membrane) and without (carried out by feed gas) the Pd_1FeO_x/aUiO(H) membrane under different feed gas flow rates (reaction condition: 25 °C, 1 hour). The error bars correspond to the standard deviation of three independent measurements.

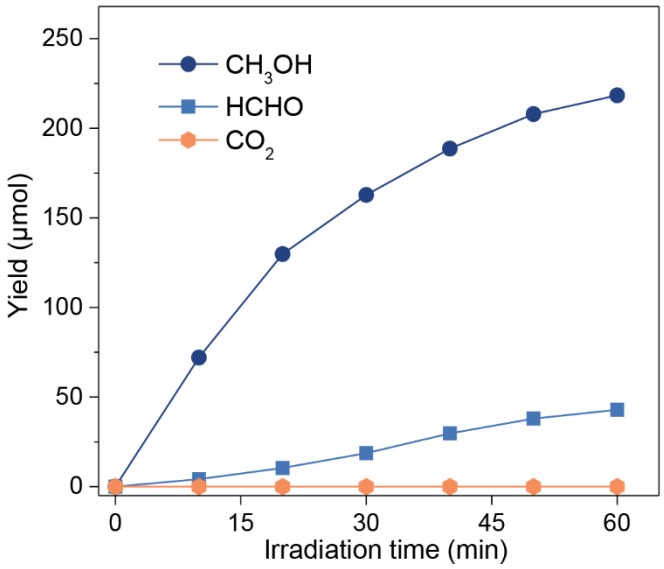

Supplementary Fig. 32: PTMO performance of Pd_1FeO_x/aUiO(H) membrane in the gas-solid system (reaction condition: 150 mL min^{-1} humidified CH_4/O_2 mixture gas, 25 °C).

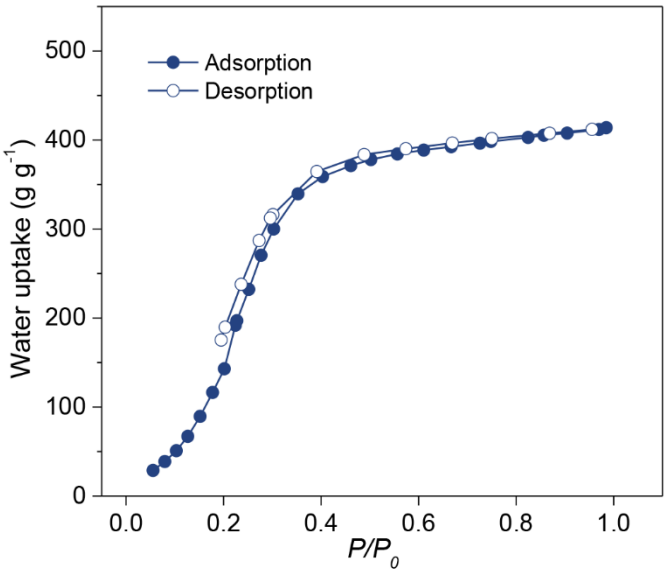

Supplementary Fig. 33: Water isotherm of Pd_1FeO_x/aUiO(H) powders at 25 °C.

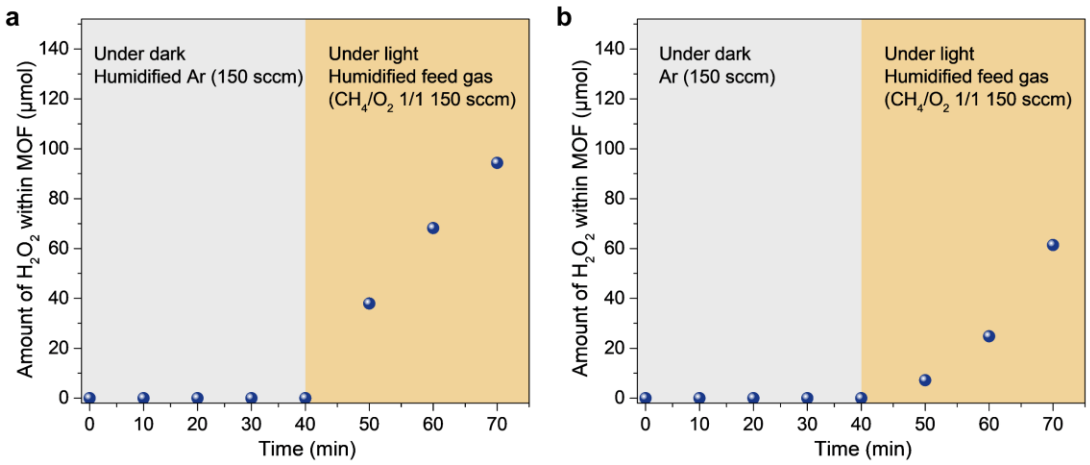

Supplementary Fig. 34: Comparison of the amount of H_2O_2 remained in Pd_1FeO_x/aUiO(H) membrane during PTMO under different mass transfer conditions (reaction condition: 25 °C) (**a**) Before the PTMO process, humidified Ar (150 mL min^{-1}) was supplied to the gas-solid system for 40 min so that some water vapor was trapped in the pores of MOF, thereby causing interface water stagnation within the MOF membrane. (**b**) Compared to the wetted gas diffusion channels (a), a gas-solid interface free from stagnant water could effectively prevent H_2O_2 dilution, thereby enhancing the utilization efficiency of the H_2O_2 intermediate.

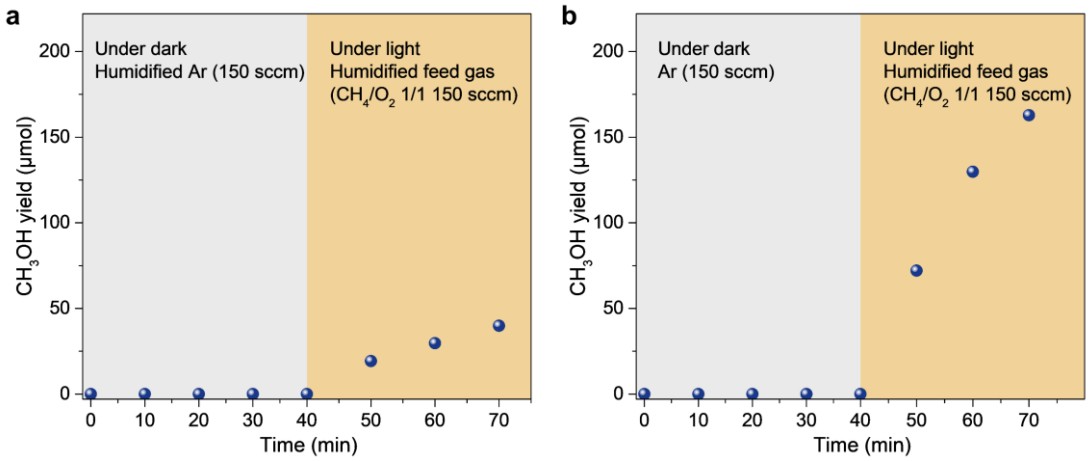

Supplementary Fig. 35: Comparison of the CH_3OH yield in the Pd_1FeO_x/aUiO(H) membrane under different mass transfer conditions corresponding to Fig. S34. Compared to the wetted gas diffusion channels (**a**), the gas-solid interface free from stagnant water could efficiently boost gas-phase PTMO (**b**).

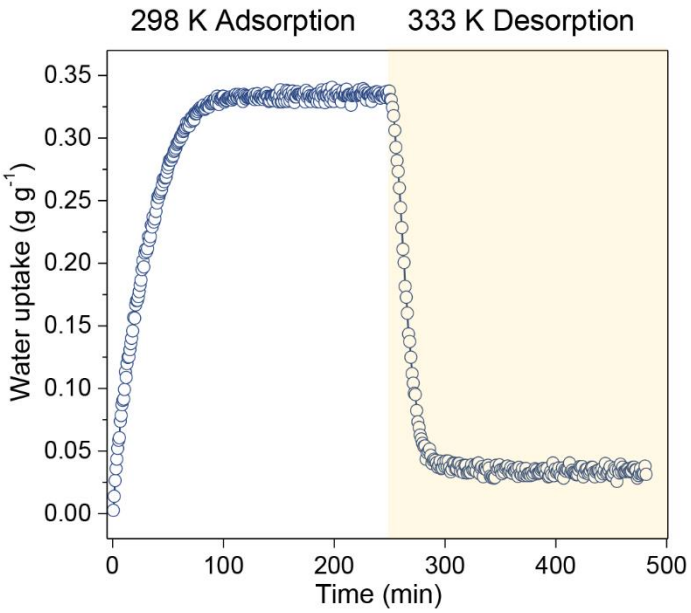

Supplementary Fig. 36: Dynamic performance of water adsorption (298 K) and desorption (333 K) for adsorbents in Pd_1FeO_x/aUiO powders with 30 % RH airflow.

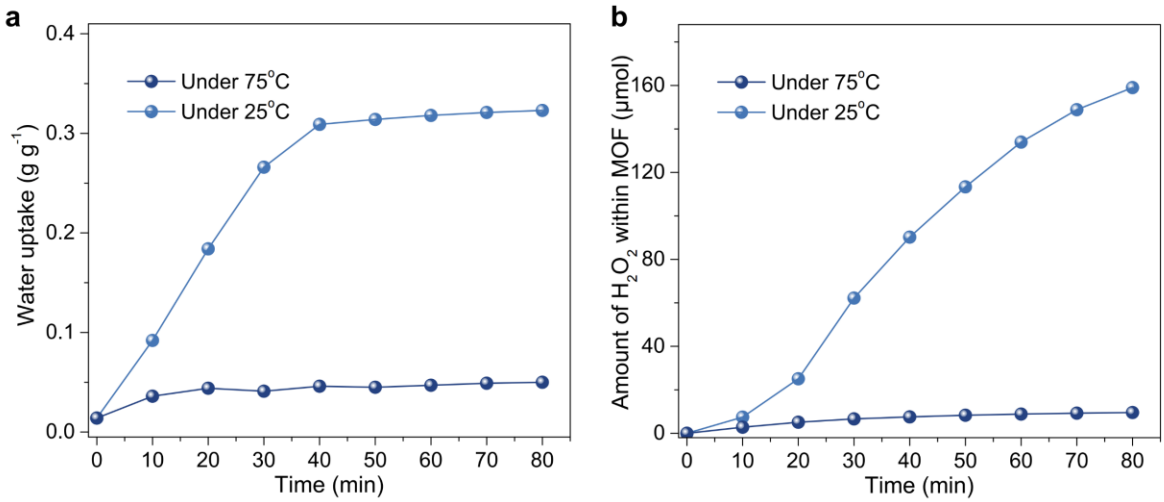

Supplementary Fig. 37: Comparison of the amount of (**a**) H_2O and (**b**) H_2O_2 remaining in the Pd_1FeO_x/aUiO(H) membrane under different system temperatures (reaction condition: 150 mL min^{-1} humidified CH_4/O_2 mixture gas).

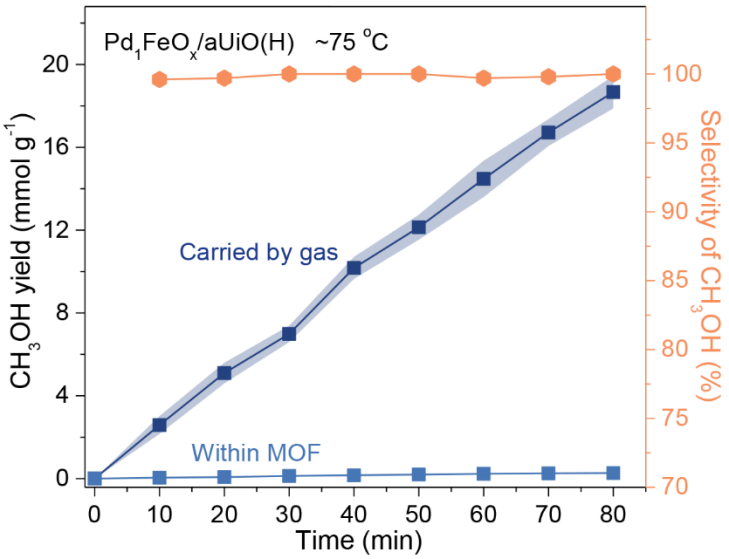

Supplementary Fig. 38: Time-on-line CH_3OH yield (left axis) and selectivity (right axis) for the Pd_1FeO_x/aUiO(H) membrane under elevated system temperature (reaction condition: 150 mL min^{-1} humidified CH_4/O_2 mixture gas, 75 °C). The error bands correspond to the standard deviation of three independent measurements.

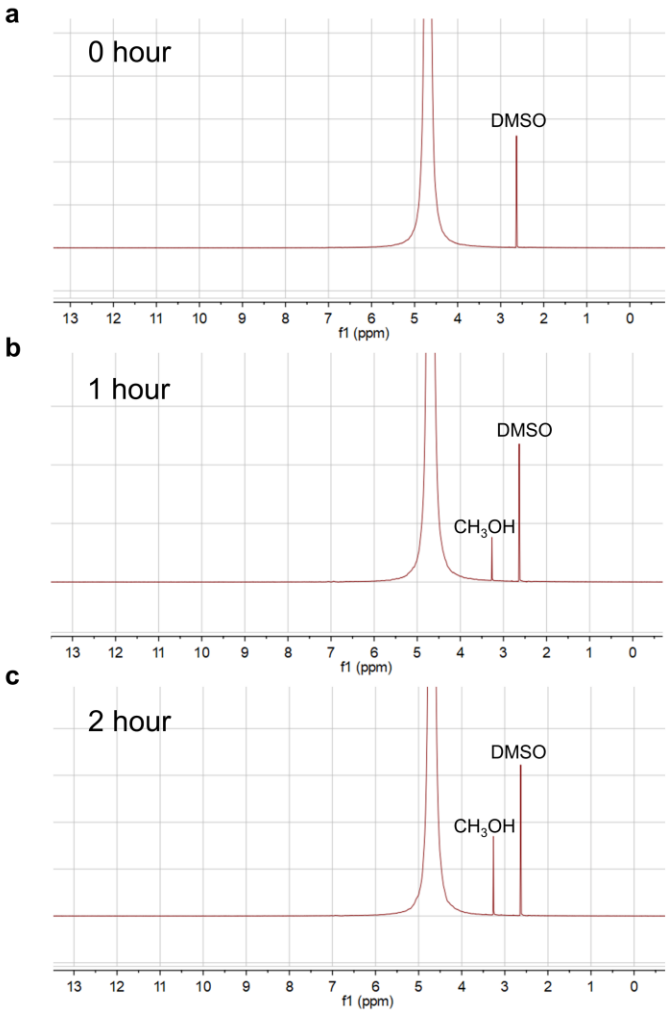

Supplementary Fig. 39: The ^{1}H NMR spectra for the liquid products of the gas-phase PTMO using Pd_1FeO_x/aUiO membrane as the catalyst after 0 h, 1 h, and 3 h reaction. The peaks at 3.27 and 2.63 ppm in the ^{1}H NMR can be assigned to CH_3OH (the oxidation product of CH_4) and DMSO (internal standard), respectively.

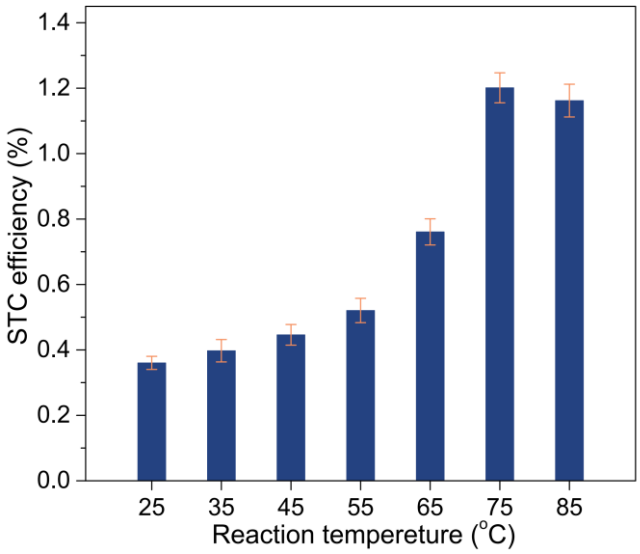

Supplementary Fig. 40: Solar-to-Chemical (STC) conversion efficiency of Pd_1FeO_x/aUiO(H) membrane under different system temperatures (reaction condition: 150 mL min^{-1} humidified CH_4/O_2 mixture gas). The error bars correspond to the standard deviation of three independent measurements.

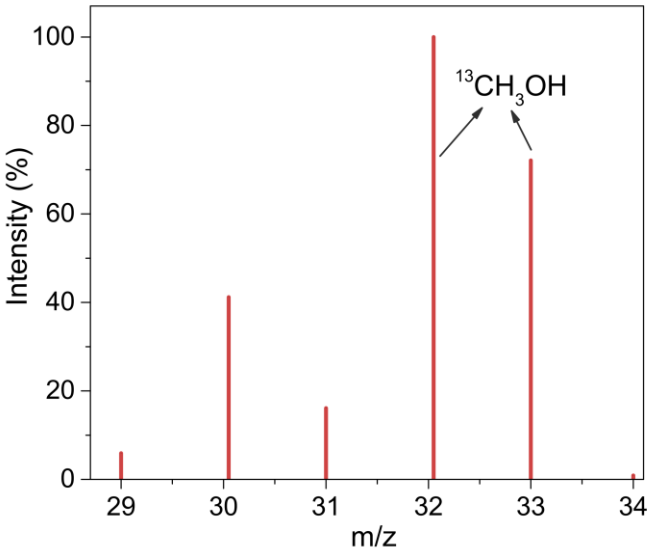

Supplementary Fig. 41: Mass spectra of the product $^{13}CH_3OH$ from $^{13}CH_4$ photo-oxidation by the Pd_1FeO_x/aUiO(H) membrane.

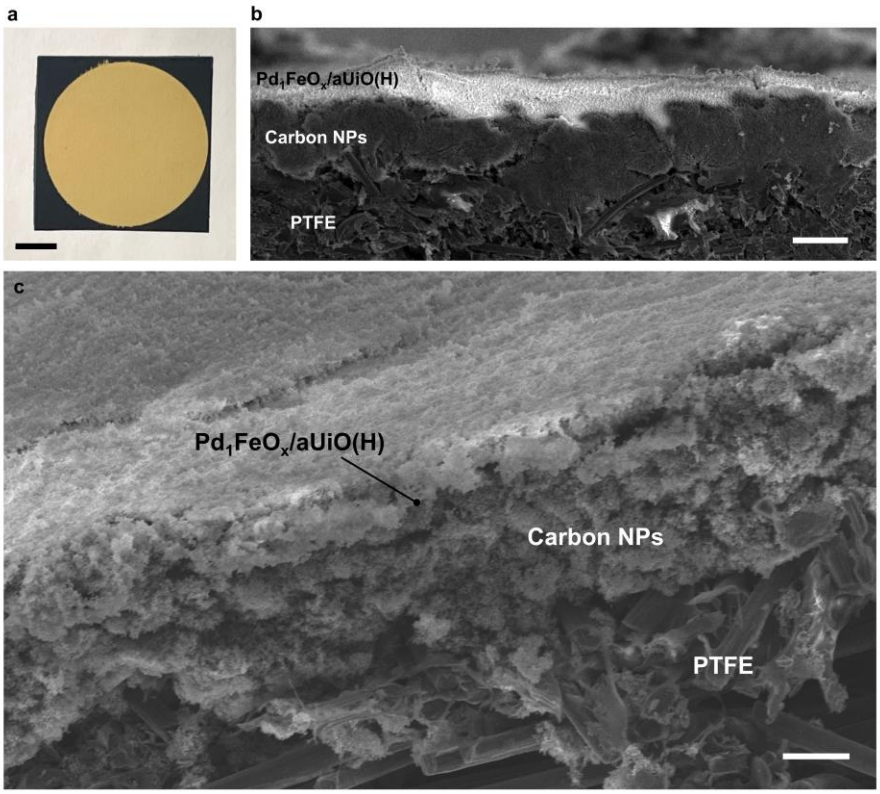

Supplementary Fig. 42: Structural characterization of the as-prepared Pd_1FeO_x/aUiO(H)/GDL membrane. (**a**) Digital photograph, (**b, c**) Cross-sectional SEM images of the Pd_1FeO_x/aUiO(H)/GDL membrane. Scale bar: (a) 1cm and (b, c) 20 μm.

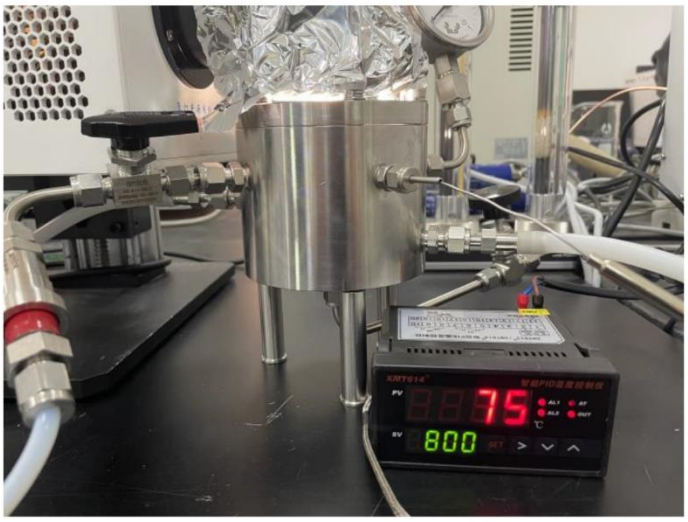

Supplementary Fig. 43: Characterization of the self-heated hybrid MOF membrane. The surface temperature of the Pd_1FeO_x/aUiO(H)/GDL membrane was maintained at roughly 75 °C during the PTMO process.

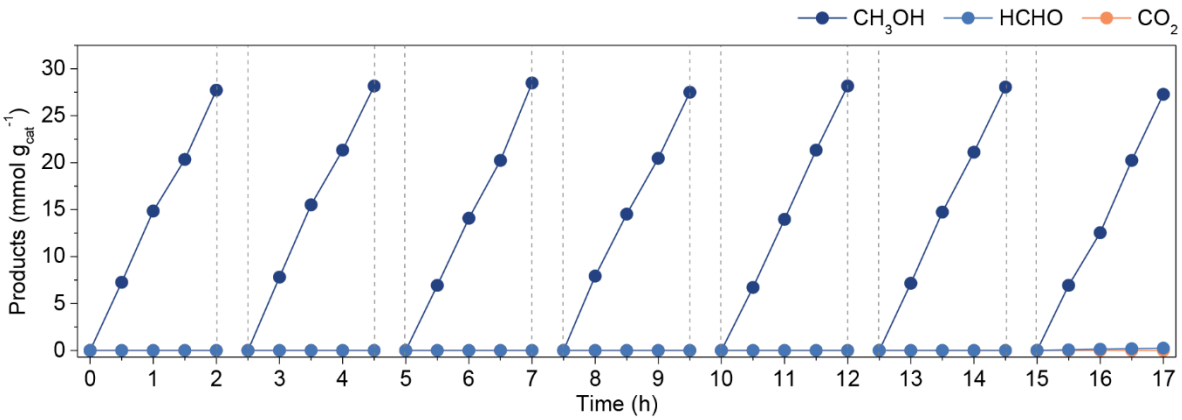

Supplementary Fig. 44: Stability test of the Pd_1FeO_x/aUiO(H)/GDL membrane under simulated sunlight irradiation (reaction condition: 150 mL min^{-1} humidified CH_4/O_2 mixture gas). Each cycle: 2 h.

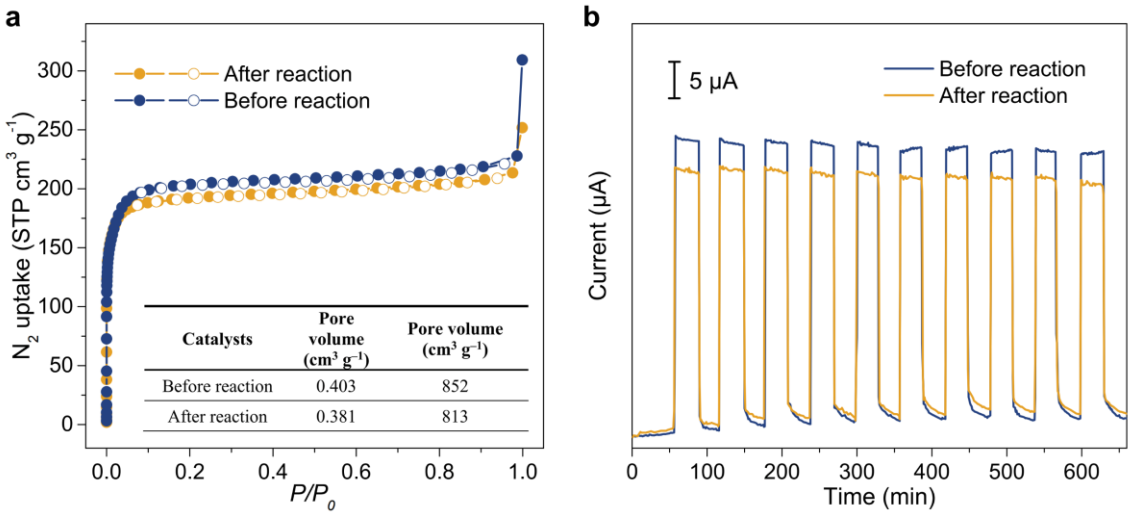

Supplementary Fig. 45: (**a**) N_2 adsorption-desorption isotherms (at 77 K) and (**b**) photocurrent-time curves under simulated sunlight irradiation for the Pd_1FeO_x/aUiO(H) catalyst before and after long-term operation (210 h).

Note: To further explore the reason behind the slight decrease in CH_3OH yield, we have conducted additional characterizations to uncover changes in the structure and photoelectric conversion efficiency of the MOF substrate following long-term reaction periods (210 h). As shown in Supplementary Fig. 45a, N_2 sorption isotherms illustrate a slight decline in both surface areas and pore volumes after long-term reaction, indicating a minor collapse in the MOF substrate's pore structure. This collapse likely diminishes the photoelectric conversion efficiency of the MOF substrate (as shown in Supplementary Fig. 45b), consequently leading to the observed slight decrease in CH_3OH yield.

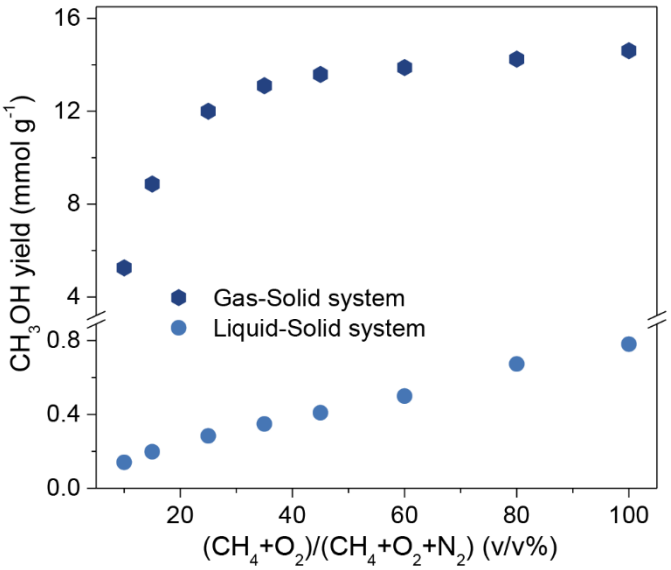

Supplementary Fig. 46: CH_3OH productivities on Pd_1FeO_x/aUiO(H) membrane (gas-solid system) and particles (liquid-solid system) under different CH_4 and O_2 concentrations (CH_4/O_2 1/1, in N_2 mixtures), respectively.

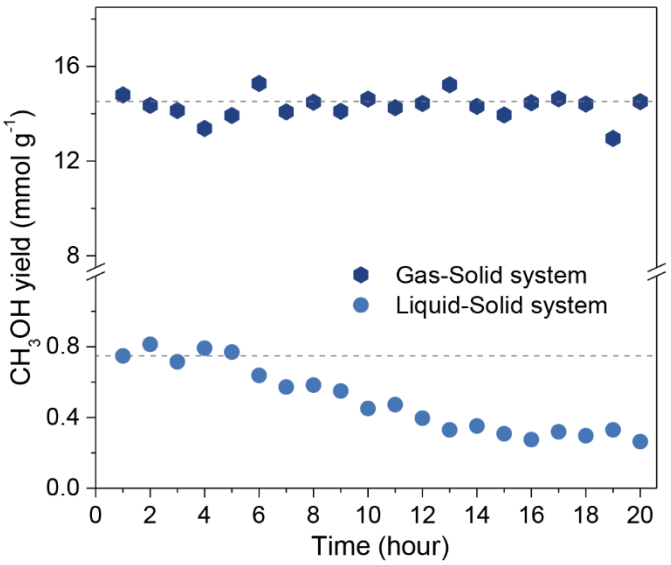

Supplementary Fig. 47: Stability test of Pd_1FeO_x/aUiO(H) catalyst under gas-solid and liquid-solid systems using tap water as the proton source.

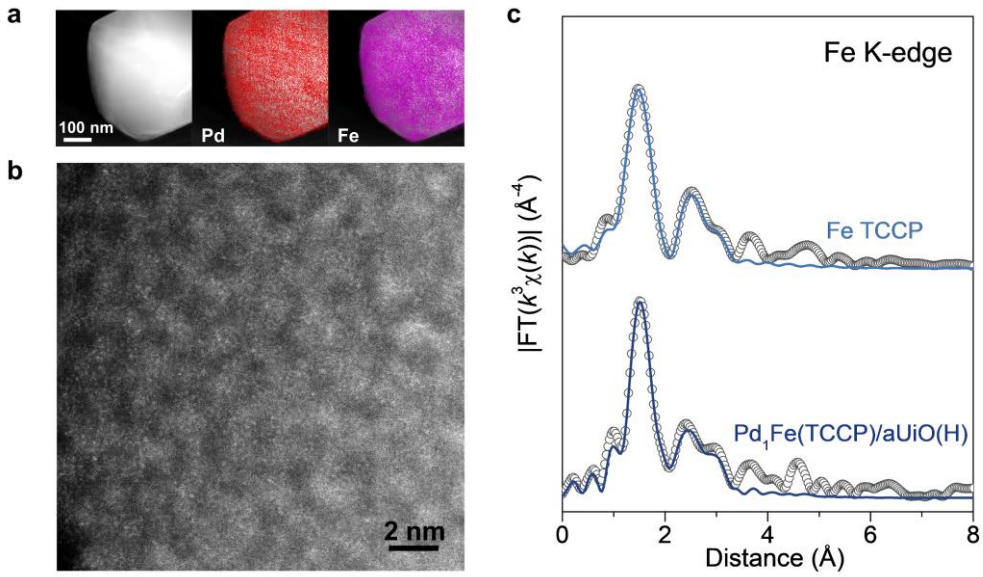

Supplementary Fig. 48: Characterization of the as-prepared Pd_1Fe(TCCP)/aUiO(H) samples. (**a**) HAADF-STEM image and corresponding EDS maps for Pd_1Fe(TCCP)/aUiO(H) particles. (**b**) AC-HAADF-STEM images for Pd_1Fe(TCCP)/aUiO(H) particles, indicating the high dispersion of metal species in the aUiO(H) matrixes. (**c**) Fe K-edge EXAFS fitting results for bare Fe TCCP and Pd_1Fe(TCCP)/aUiO(H) particles. The presence of only one notable peak in the region of 1 to 2 Å indicates the existence of only Fe–N contribution, confirming the atomic dispersion of Fe species in the Pd_1Fe(TCCP)/aUiO(H) samples.

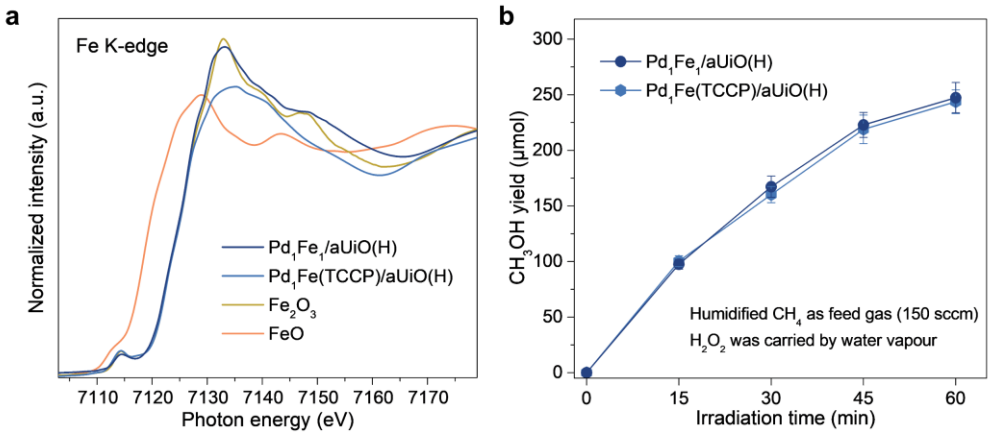

Supplementary Fig. 49: Comparison of the electronic structure and intrinsic HMO activity of the Fe sites in the Pd_1Fe(TCCP)/aUiO(H) and Pd_1Fe_1/aUiO(H) catalysts. (**a**) Fe K-edge XANES spectra of Pd_1Fe(TCCP)/aUiO(H) and Pd_1Fe_1/aUiO(H) samples, with Fe_2O_3 and FeO as references, highlighting the similar electronic structure of Fe sites in both the Pd_1Fe(TCCP)/aUiO(H) and Pd_1Fe_1/aUiO(H) catalysts. (**b**) Photocatalytic CH_4 oxidation activity of Pd_1Fe(TCCP)/aUiO(H) and Pd_1Fe_1/aUiO(H) samples under ambient temperature. During the tests, none of the oxygen was introduced. The H_2O_2, as the initiator of HMO, was carried into the reaction system by the humidified CH_4/Ar (v/v=1/1) mixture gas (150 mL min^{-1}). The similar CH_3OH yield in the Pd_1Fe(TCCP)/aUiO(H) and Pd_1Fe_1/aUiO(H) membrane indicates that these two samples possess similar HMO activity.

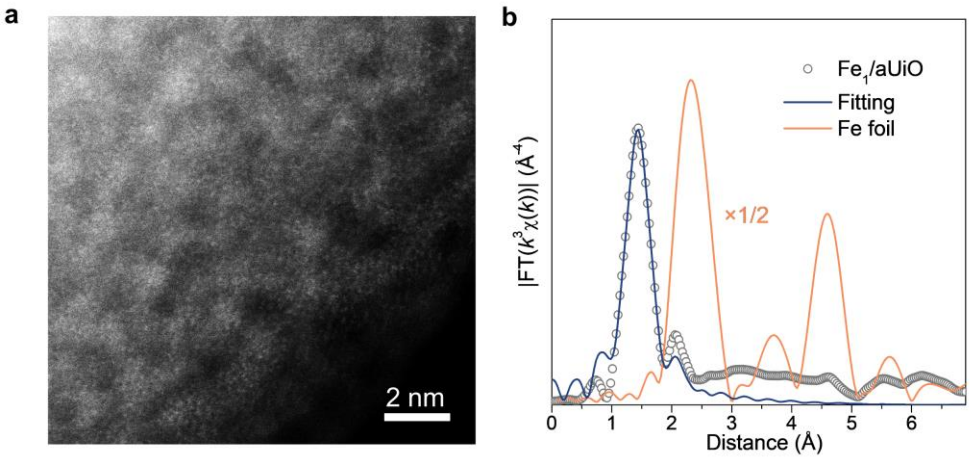

Supplementary Fig. 50: Structural characterization of the as-prepared Fe_1/aUiO catalyst. (**a**) AC-HAADF-STEM image for Fe_1/aUiO particles. (**b**) Fe K-edge EXAFS fitting results for Fe_1/aUiO particles. The presence of only one notable peak in the region of 1 to 2 Å indicates the existence of only Fe–O contribution with no Fe–Fe contribution (in the region of 2 to 3 Å), confirming the atomic dispersion of Fe species in the Fe_1/aUiO sample.

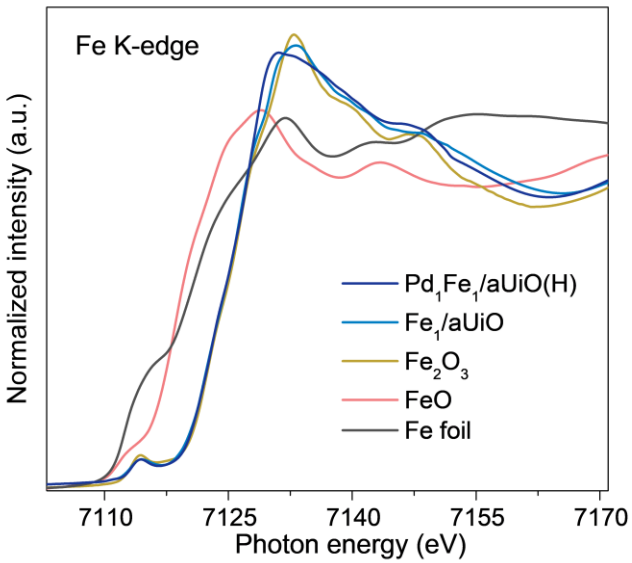

Supplementary Fig. 51: Fe K-edge XANES spectra of Pd_1Fe_1/aUiO(H) and Fe_1/aUiO catalysts, with Fe_2O_3, FeO, and Fe foil as references.

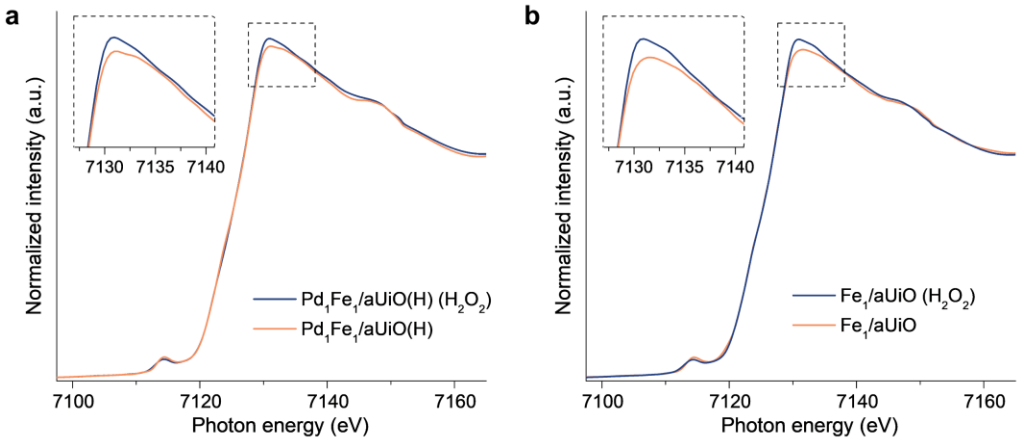

Supplementary Fig. 52: Fe K-edge XANES spectra of pristine and H_2O_2-treated catalysts. (**a**) Pd_1Fe_1/aUiO(H). (**b**) Fe_1/aUiO.

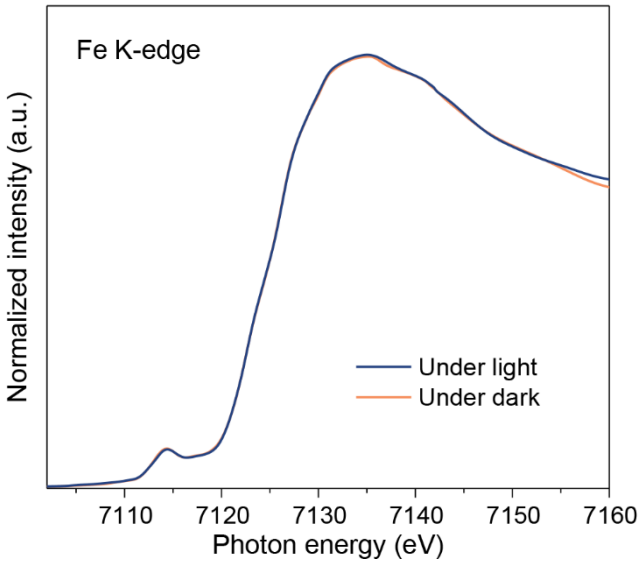

Supplementary Fig. 53: In situ Fe K-edge XANES spectra of Pd_1Fe(TCCP)/aUiO(H) catalyst under PTMO conditions.

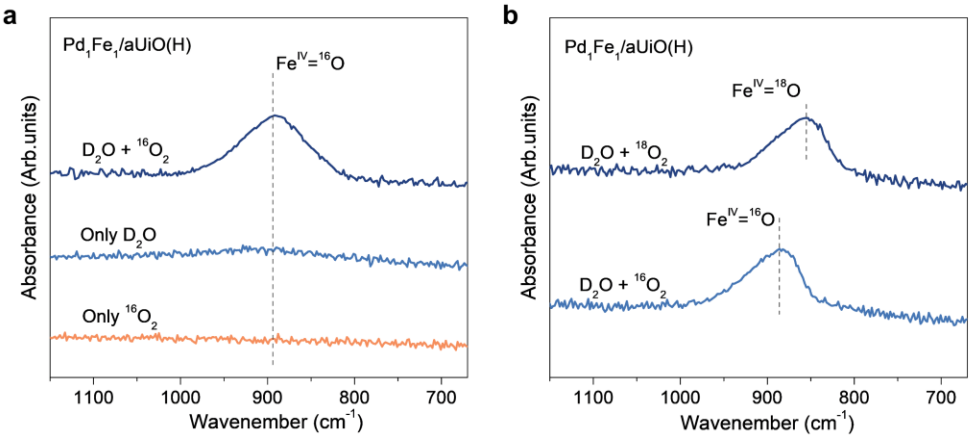

Supplementary Fig. 54: In situ ATR-FTIR spectra of Pd_1Fe_1/aUiO catalyst under PTMO conditions. (**a**) Using $^{16}O_2$ as the oxygen source. (**b**) Using $^{18}O_2$ as the oxygen source. The absorption peaks at 886.3 cm^{-1} and 855.4 cm^{-1} to be assigned to $Fe^{IV}=^{16}O$ and $Fe^{IV}=^{18}O$ species, respectively. Indicating that the oxidation of Fe_1 sites to Fe^{IV}=O active species was induced by the H_2O_2 generated on the Pd_1 sites from oxygen and water.

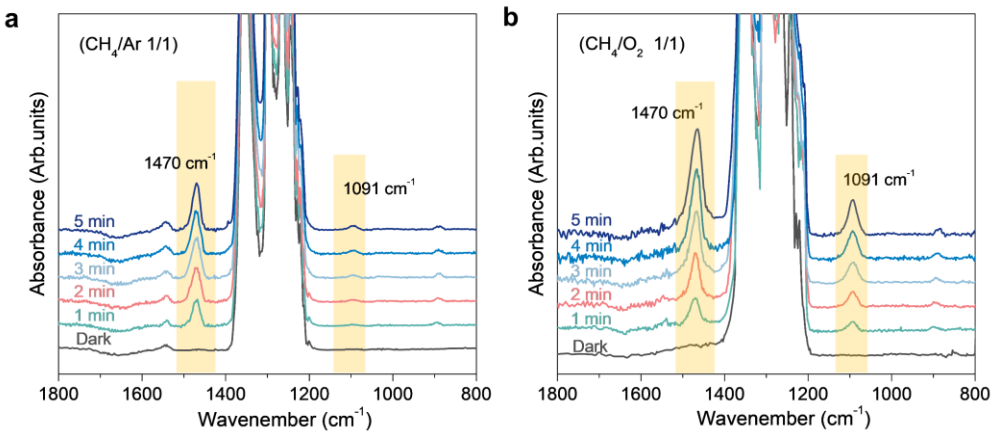

Supplementary Fig. 55: In situ ATR-FTIR spectra of Pd_1FeO_x/aUiO(H) catalyst under PTMO conditions. (**a**) Humidified CH_4/Ar (v/v=1/1) mixture as the feed gas. (**b**) humidified CH_4/O_2 (v/v=1/1) mixture as the feed gas.

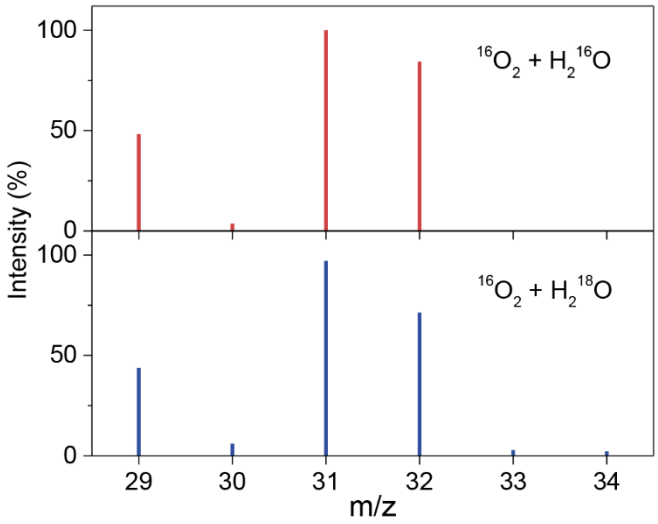

Supplementary Fig. 56: Isotope-labelled experiments for methanol production in the presence of isotope-labelled $H_2{}^{18}O$. Nearly no isotope-labelled $CH_3{}^{18}OH$ (m/z = 33 and 34) was detected by GCMS, suggesting O_2 was the only oxygen source for CH_3OH formation.

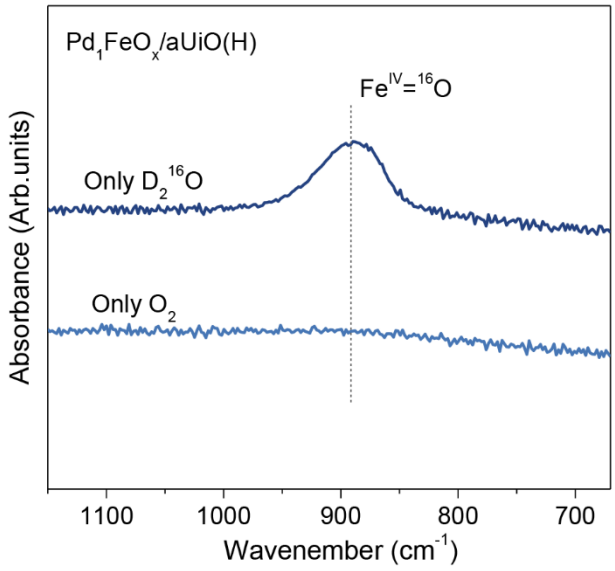

Supplementary Fig. 57: In situ ATR-FTIR spectra of Pd_1FeO_x/aUiO catalyst under PTMO conditions. The absorption peaks at 886.3 cm^{-1} to be assigned to $Fe^{IV}=^{16}O$ species. Indicating that the Fe^{IV}=O active species were formed on the iron oxide clusters through a photo-oxidation process in the presence of water.

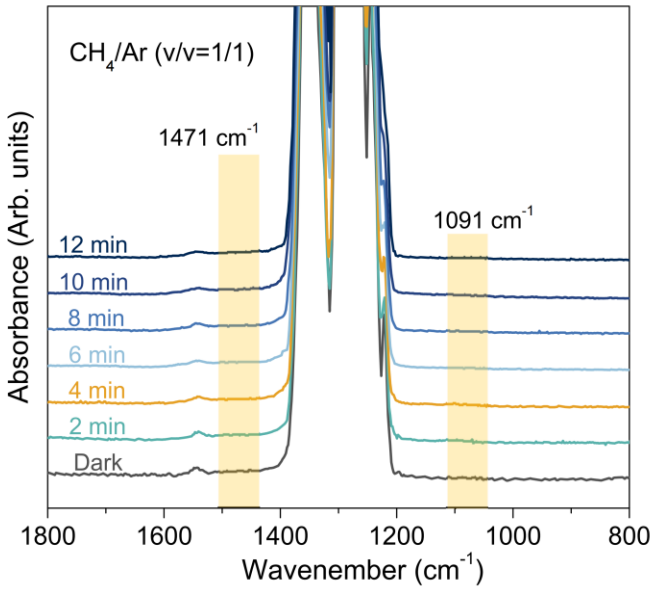

Supplementary Fig. 58: In situ ATR-FTIR spectra of Pd_1Fe_1/aUiO(H) catalyst under photocatalytic CH_4 oxidation conditions by using an anhydrous CH_4/Ar mixture as feed gas.

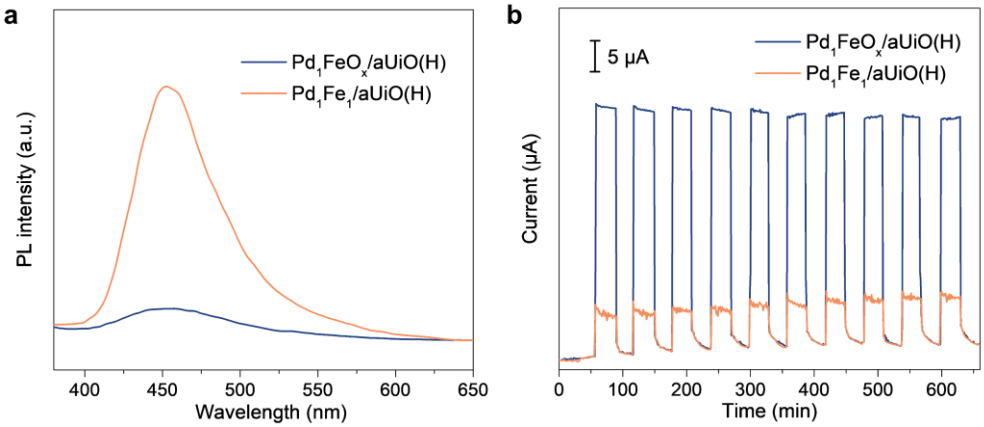

Supplementary Fig. 59: Characterizations of the Pd_1FeO_x/aUiO(H) and Pd_1Fe_1/aUiO(H) catalysts show the suppression of photogenerated carrier recombination by the FeO_x species. (**a, b**) Steady-state photoluminescence (PL) spectra (**a**) and photocurrent-time curves under simulated sunlight irradiation (**b**) for Pd_1FeO_x/aUiO(H) and Pd_1Fe_1/aUiO(H). The decoration of FeO_x species as the photohole acceptor could effectively boost the separation of photoexcited electron-hole pairs.

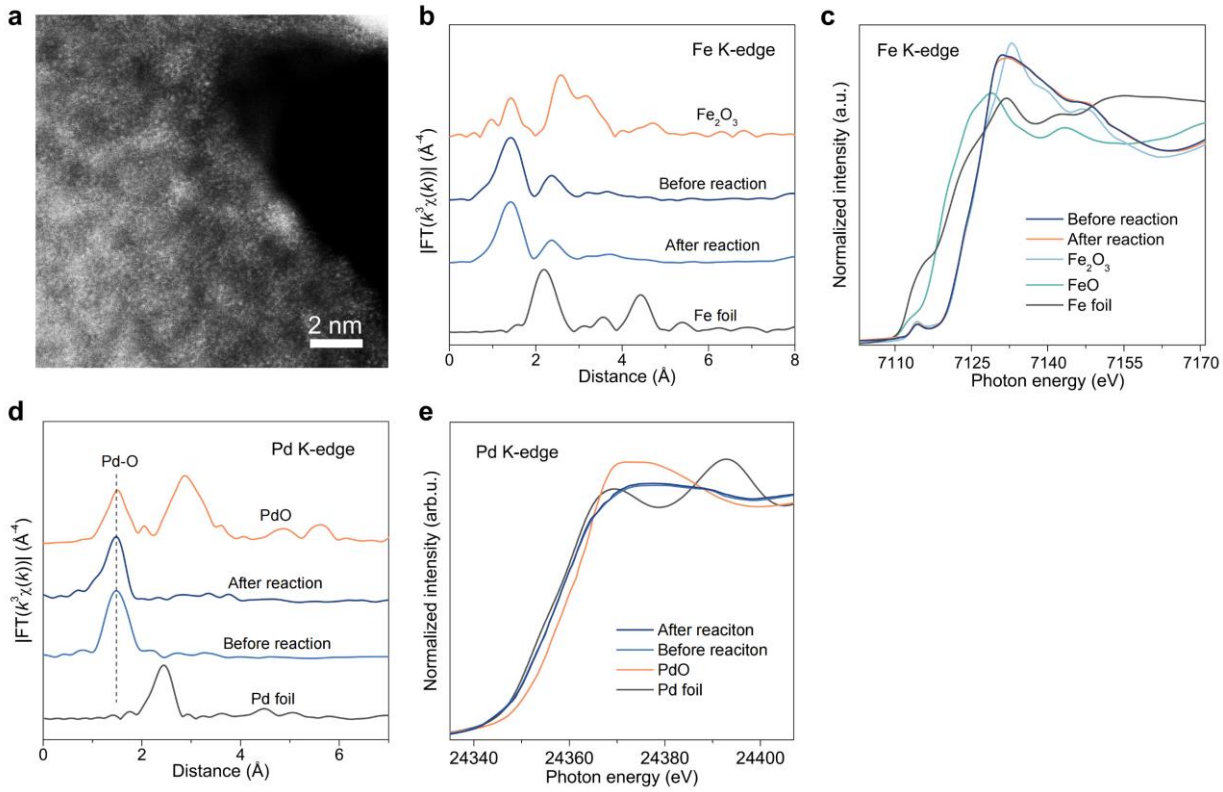

Supplementary Fig. 60: Characterization of the Pd_1FeO_x/aUiO(H) catalyst after long-term operation (210 h). (**a**) AC-HAADF-STEM image. (**b, c**) Fe K-edge EXAFS spectra (**b**) and Fe K-edge XANES spectra (**c**) of Pd_1FeO_x/aUiO(H) catalyst before and after long-term operation. (**d, e**) Pd K-edge EXAFS spectra (**d**) and XANES spectra (**e**) of Pd_1FeO_x/aUiO(H) catalyst before and after long-term operation.

Supplementary Table 1: The surface areas and pore volumes of Pd_1FeO_x/aUiO(H), Pd_1Fe_1/aUiO(H), and Pd_1/aUiO(H) samples. The pore size model is "N_2 at 77 K on carbon (slit pore, NLDFT equilibrium model)".

Catalysts	Pore volume ($cm^3\ g^{-1}$)	Surface areas ($m^2\ g^{-1}$)
Pd_1FeO_x/aUiO(H)	0.403	852
Pd_1Fe_1/aUiO(H)	0.420	1060
Pd_1/aUiO(H)	0.421	1068

Supplementary Table 2: EXAFS fitting results for as-obtained catalysts.

Catalysts	Shell	Coordination number	*R*(Å)	$\sigma^2/\times10^{-3}$(Å^2)
Pd_1FeO_x/aUiO(H)	Pd–O	2.8 ± 0.6	2.02 ± 0.01	3.7 ± 1.0
	Pd–Pd	–	–	–
	Fe–O	6.3 ± 0.5	1.97 ± 0.01	4.2 ± 1.7
	Fe–Fe	3.0 ± 0.3	3.02 ± 0.01	7.0 ± 1.2
Pd_1Fe_1/aUiO(H)	Pd–O	2.6 ± 0.7	2.52 ± 0.02	2.9 ± 1.1
	Pd–Pd	–	–	–
	Fe–O	6.2 ± 0.7	1.96 ± 0.02	8.0 ± 1.6
	Fe–Fe	–	–	–
Pd_1/aUiO(H)	Pd–O	2.8 ± 0.5	2.72 ± 0.02	4.7 ± 1.6
	Pd–Pd	–	–	–
Pd_1/aUiO	Pd–O	3.8 ± 0.5	2.04 ± 0.01	2.8 ± 1.2
	Pd–Pd	–	–	–
Fe_1/aUiO	Fe–O	6.3 ± 0.5	2.01 ± 0.01	2.4 ± 1.2
	Fe–Fe	–	–	–

σ^2: Debye-Waller factor (a measure of thermal and static disorder in absorber-scatterer distances). ΔE_0 is the edge energy shift (the difference between the zero kinetic energy value of the sample and that of the theoretical model).

Supplementary Table 3: Comparison of the reported catalysts for photo-oxidation of CH_4 to CH_3OH.

Catalysts	Oxidant	Light intensity ($mW\ cm^{-2}$)	Time (h)	CH_3OH yield ($\mu mol\ g_{cat}^{-1}h^{-1}$)	CH_3OH selectivity (%)	Ref.
Pd_1FeO_x/aUiO(H) membrane	**O_2**	**100**	**215**	**14400**	**100**	**This work**
PMOF-RuFe(OH) (flow)	O_2	–	120	8810	100	1
0.1 wt% Au/ZnO	O_2	100	2	2060	15.7	2
0.1 wt% Pd/ZnO	O_2	100	2	3035	26.2	
0.1 wt% Pt/ZnO	O_2	100.	2	2225	19.1	
30CW (C_3N_4-$Cs_{0.33}WO_3$)	O_2	–	4	4.375	38.1	3
Au_1/BP	O_2	382	2	56.8	99	4
q-$BiVO_4$ (10 mL of H_2O)	O_2	170	3	971	62.8	5
	O_2	170	3	370	96.6	
$BiVO_4$	H_2O	170	2	21	48	
$BiVO_4$ thick platelet	H_2O	–	2	79.2	85.7	6
$BiVO_4$ bipyramids	H_2O	–	2	111.9	85	
Cu-0.5/PCN	H_2O	–	1	5.5	12.8	7
commercial V_2O_5	H_2O	–	2	2.0	100	8
V-HBEA	H_2O	–	2	11.3	85.4	
Bi-V-HBEA	H_2O	–	2	10.7	100	
Ag/InGaN	H_2O	5000	4	45500	92	9
Au–Pd/TiO_2	H_2O	250	1	12556	42.3	10
WO_3/Fe^{3+} (2mM)	H_2O	–	2	55.5	37.4	11
WO_3/Cu^{2+} (0.1mM)	H_2O	–	2	46.0	38.4	
WO_3/Ag^{+} (2mM)	H_2O	–	2	16.8	11.8	
WO_3	H_2O	–	2	5.1	22	
0.12_{metal} wt%AuO/TiO_2	H_2O_2	–	3	53.3	32	12
0.33_{metal} wt%Cu_2O/TiO_2	H_2O_2	–	3	6.7	3	
0.47 wt% Fe_2O_3/TiO_2	H_2O_2	–	3	357	89	
0.33_{metal} wt% FeO_x/TiO_2	H_2O_2	–	3	360	79	
0.6 μmol $FeCl_2$	H_2O_2	–	3	1.3	20	
pristine m-WO_3	H_2O_2	82	4	19.8	25	13
1.98% FeOOH/m-WO_3	H_2O_2	82	4	211.2	91	
g-CN	H_2O_2	100	2	140	63	14

Supplementary Table 4: Comparison of state-of-art thermocatalysts for oxidation of CH_4 to CH_3OH.

Catalysts	Oxidant	T (°C)	Continuous operation time (h)	CH_3OH productivity ($\mu mol \cdot h^{-1}$)	CH_3OH yield ($mmol \cdot g_{metal}^{-1} h^{-1}$)	CH_3OH selectivity (%)	Ref.
Pd_1FeO_x/aUiO(H) membrane	**O_2**	**~73[a]**	**215**	**720**	**862.3**	**100**	**This work**
Pd_3Au_1 NS	O_2	70	0.5	147.8	147.8	98	15
AuPd@ZSM-5-C16	O_2	70	0.5	127.44	90.0	92	16
PdCu/ZSM-5	H_2O_2	80	0.5	28.35	90	56	17
Au-Pd/TiO_2	O_2	50	0.5	15.2	53.6	92	18
Rh/Pt/Ni-MMZ-IMP	O_2	150	3.0	0.12	1.2	70	19
Rh-ZSM-5	O_2+CO	150	6.0	24.48	28.6	55.4	20
AuPd/TiO_2	O_2	50	0.5	8.96	1.18	79.4	21
Au-ZSM-5	O_2	240	2.0	13.7	27.4	44.2	22
Au_1/BP	O_2	90	2.0	11.36	56.75	99	4
Ru_xCu_{1-x} ILs/SiO_2-200	O_2	50	1.0	0.11	2.25	93.8	23

[a] Using infrared light from the solar spectrum to heat the catalyst layer to ~73 °C directly, eliminating all extra energy consumption for maintaining the membrane temperature.

Supplementary Table 5: ICP analysis of Pd_1FeO_x/aUiO(H) photocatalyst membrane before and after PTMO reactions.

Reaction time (hour)	Loading (wt.%)	
	Pd	Fe
0	0.78	0.89
100	0.78	0.89
210	0.78	0.88

References

1. An, B., Li, Z. & Wang, Z. et al. Direct photo-oxidation of methane to methanol over a mono-iron hydroxyl site. *Nat. Mater.* **21**, 932–938 (2022).
2. Song, H. et al. Direct and selective photocatalytic oxidation of CH_4 to oxygenates with O_2 on cocatalysts/ZnO at room temperature in water. *J. Am. Chem. Soc.* **141**, 20507–20515 (2019).
3. Li, Y., Li, J., Zhang, G., Wang, K. & Wu, X. Selective photocatalytic oxidation of low concentration methane over graphitic carbon nitride-decorated tungsten bronze cesium. *ACS Sustainable Chem. Eng.* **7**, 4382–4389 (2019).
4. Luo, L. et al. Water enables mild oxidation of methane to methanol on gold single-atom catalysts. *Nat. Commun.* **12**, 1218 (2021).
5. Fan, Y. et al. Selective photocatalytic oxidation of methane by quantum-sized bismuth vanadate. *Nat. Sustain* **4**, 509–515 (2021).
6. Zhu, W. L. et al. Facet-dependent enhancement in the activity of bismuth vanadate microcrystals for the photocatalytic conversion of methane to methanol. *ACS Appl. Nano Mater.* **1**, 6683–6691 (2018).
7. Zhou, Y. et al. Direct functionalization of methane into ethanol over copper modified polymeric carbon nitride via photocatalysis. *Nat. Commun.* **10**, 506 (2019).
8. Murcia-Lopez, S. et al. Controlled photocatalytic oxidation of methane to methanol through surface modification of beta zeolites. *ACS Catal.* **7**, 2878–2885 (2017).
9. Zhou, P., Tang, S. T., Ye, Z. W. & Mi. Z. T. Water-promoted selective photocatalytic methane oxidation for methanol production. *Chem. Sci.***15**, 1505–1510 (2024).
10. Cai, X., Fang, S. & Hu, Y. H. Unprecedentedly high efficiency for photocatalytic conversion of methane to methanol over Au–Pd/TiO_2 – what is the role of each component in the system? *J. Mater. Chem. A* **9**, 10796–10802 (2021).
11. Villa, K., Murcia-Lopez, S., Andreu, T. & Morante, J. R. On the role of WO_3 surface hydroxyl groups for the photocatalytic partial oxidation of methane to methanol. *Catal. Commun.* **58**, 200–203 (2015).
12. Xie, J. et al. Highly selective oxidation of methane to methanol at ambient conditions by titanium dioxide-supported iron species. *Nat. Catal.* **1**, 889 (2018).
13. Yang, J., Hao, J., Wei, J., Dai, J. & Li, Y. Visible-light-driven selective oxidation of methane to methanol on amorphous FeOOH coupled m-WO_3. *Fuel* **266**, 117104 (2020).
14. Shi, S., Sun, Z., Bao, C., Gao, T. & Hu, Y. H. The special route toward conversion of methane to methanol on a fluffy metal-free carbon nitride photocatalyst in the presence of H_2O_2. *Int. J. Energy Res.* **44**, 2740–2753 (2020).
15. Xu, Y., Wu, D., Zhang, Q. *et al.* Regulating Au coverage for the direct oxidation of methane to methanol. *Nat. Commun*. **15**, 564 (2024).
16. Jin, Z. *et al.* Hydrophobic zeolite modification for in situ peroxide formation in methane oxidation to methanol. *Science* **367**, 193–197 (2020).
17. Wu, B., et al., Tandem catalysis for selective oxidation of methane to oxygenates using oxygen over PdCu/Zeolite. *Angew. Chem., Int. Ed.* **61**, e202204116 (2022).

18. Agarwal, N. *et al.* Aqueous Au-Pd colloids catalyze selective CH_4 oxidation to CH_3OH with O_2 under mild conditions. *Science* **358**, 223–227 (2017).

19. Jia, X., et al., Library creation of ultrasmall multi-metallic nanoparticles confined in mesoporous MFI zeolites. *Angew. Chem., Int. Ed*. **60**, 14571–14577 (2021).

20. Shan, J., Li, M., Flytzani-Stephanopoulos, M., Allard, L. F. & Lee, S. Mild oxidation of methane to methanol or acetic acid on supported isolated rhodium catalysts. *Nature* **551**, 605–608 (2017).

21. Ab Rahim, M. H. *et al.* Oxidation of methane to methanol with hydrogen peroxide using supported gold–palladium alloy nanoparticles. *Angew. Chem. Int. Ed.* **52**, 1280–1284 (2013).

22. Qi, G., et al., Au-ZSM-5 catalyses the selective oxidation of CH_4 to CH_3OH and CH_3COOH using O_2. *Nat. Catal.* **5**, 45–54 (2022).

23. Bai, S., Yao, Q., Xu, Y., Cao, K. & Huang, X. Strong synergy in a lichen-like RuCu nanosheet boosts the direct methane oxidation to methanol. *Nano Energy* **71**, 104566 (2020).